Highlights

TransLK-Net: Entangling Transformer and Large Kernel for Progressive and Collaborative Feature Encoding and Decoding in Medical Image Segmentation

Jin Yang, Daniel S. Marcus, Aristeidis Sotiras

- We propose novel Progressively Entangled Transformer Large Kernel and Collaboratively Entangled Transformer Large Kernel modules to leverage the benefits of large kernel convolutions and transformer self-attention for generic local and global feature extraction.
- We propose a novel Attention-gated Channel MLP to equip MLP with the capabilities of capturing pixel-wise spatial information, thus improving its representation powers for segmentation.
- We propose a Cross Entanglement Decoding block for efficient feature fusion and information decoding. It employs
 Progressive Feature Interaction and Collaborative Feature Interaction modules to fuse features from the decoder and
 skip-connected from the encoder, avoiding semantic gaps during fusion.
- We propose a novel network for volumetric medical image segmentation, termed TransLK-Net by incorporating
 these modules into a hierarchical ViT-based encoder-decoder architecture. It achieved superior performance with low
 computational complexity compared to other SOTA methods in four heterogeneous volumetric segmentation tasks.

TransLK-Net: Entangling Transformer and Large Kernel for Progressive and Collaborative Feature Encoding and Decoding in Medical Image Segmentation

Jin Yang^a, Daniel S. Marcus^a and Aristeidis Sotiras^{a,b,**}

ARTICLE INFO

Keywords: Large Kernel Convolution Vision Transformer Feature Encoding and Decoding Channel and Spatial Attention Medical Image Segmentation

ABSTRACT

Convolutional neural networks (CNNs) and vision transformers (ViTs) are widely employed for medical image segmentation, but they are still challenged by their intrinsic characteristics. CNNs are limited from capturing varying-scaled features and global contextual information due to the employment of fixed-sized kernels. In contrast, ViTs employ self-attention and MLP for global information modeling, but they lack mechanisms to learn spatial-wise local information. Additionally, selfattention leads the network to show high computational complexity. To tackle these limitations, we propose Progressively Entangled Transformer Large Kernel (PTLK) and Collaboratively Entangled Transformer Large Kernel (CTLK) modules to leverage the benefits of self-attention and large kernel convolutions and overcome shortcomings. Specifically, PTLK and CTLK modules employ the Multihead Large Kernel to capture multi-scale local features and the Efficient Decomposed Self-attention to model global information efficiently. Subsequently, they employ the Attention Entanglement mechanism to enable local and global features to enhance and calibrate each other progressively and collaboratively. Additionally, an Attention-gated Channel MLP (AG-MLP) module is proposed to equip the standard MLP module with the capabilities of modeling spatial information. PTLK and CTLK modules are further incorporated as a Cross Entanglement Decoding (CED) block for efficient feature fusion and decoding. Finally, we propose a novel network for volumetric medical image segmentation that employs an encoder-decoder architecture, termed TransLK-Net. The encoder employs a hierarchical ViT architecture whose block is built by incorporating PTLK and CTLK with AG-MLP into a ViT block, and the decoder employs the CED block. TransLK-Net was evaluated on four heterogeneous volumetric medical image segmentation tasks and achieved superior performance than other state-of-the-art methods with lower computational complexity. The code is made available at https://github.com/sotiraslab/TransLK-Net.

1. Introduction

Segmentation of organs and lesions in medical images supports clinical workflows, including diagnosis, prognosis, and treatment. However, manual annotation or contouring is labor-intensive and error-prone, motivating the development of automatic tools to improve efficiency and avoid errors (Wang et al., 2021a). Deep learning (DL) techniques have revolutionized this field and various DL-based automatic segmentation methods have been developed with great success. Among these methods, convolutional neural networks (CNNs), especially U-Net (Ronneberger et al., 2015) and its variants (Zhou et al., 2018; Schlemper et al., 2019; Huang et al., 2020; Isensee et al., 2021; Yang et al., 2025b), are widely applied for automatic medical image segmentation. These methods are proposed for organ or tissue segmentation in various medical image modalities, e.g., Computed Tomography (CT) (Minnema et al., 2018; Yang et al., 2023; Zhou et al., 2024; Yang et al., 2025d), Magnetic Resonance (MR) (Moeskops et al., 2016; Fu et al., 2018), Positron Emission Tomography (PET) (Zhao et al., 2018), X-ray

ORCID(s):

(Bullock et al., 2019; Kónya et al., 2021), and Electronic Microscopy (EM) (Oztel et al., 2017; Khadangi et al., 2021).

However, CNN-based methods are still challenged in various medical image segmentation tasks. First, CNNs are challenged to capture multi-scale features due to their employment of convolutional layers with a fixed-sized kernel (Cai et al., 2016). Thus, they are limited from modeling complex structures and large inter-subject variations in shape and size, resulting in inferior segmentation performance. Several methods have been proposed to improve CNNs by equipping them with capabilities to capture multi-scale features, such as feature pyramid networks (Lin et al., 2017; Seferbekov et al., 2018; Zhao et al., 2019) and multi-branch segmentation networks (Aslani et al., 2019; Chen et al., 2022). However, these prior works change the macro-architecture of CNNs and may not be readily integrated into general CNN structures, limiting their applicability. Other methods employ several convolutional layers with different kernel sizes to extract multi-scale features in the same level (Yin et al., 2023; Alam et al., 2022; Yang et al., 2025a). However, features from the same channel are extracted repeatedly by multiple convolutional layers, leading to redundant use of computational resources and model parameters (Lin et al., 2023). Second, CNNs fail to utilize global contextual information outside the receptive field to model long-range

^aMallinckrodt Institute of Radiology, Washington University School of Medicine in St. Louis, St. Louis, 63110, MO, USA

^bInstitute for Informatics, Data Science and Biostatistics, Washington University School of Medicine in St. Louis, St. Louis, 63110, MO, USA

^{**}Corresponding author

yang.jin@wustl.edu (J. Yang); aristeidis.sotiras@wustl.edu (A. Sotiras)

dependencies among features when convolutional layers extract features within local kernel windows (Bello et al., 2019).

Compared with CNNs, Vision Transformers (ViTs) model long-range dependencies by employing the attention mechanism (e.g., self-attention and cross-attention) (Dosovitskiy et al., 2021). This mechanism empowers ViT-based models with image-level receptive fields to utilize global contextual information across the entire input image (Fan et al., 2024). However, ViT-based models are challenged by intrinsic characteristics of the attention mechanism to achieve superior segmentation performance in medical images. Specifically, self-attention processes 1D input sequences without localization information, lowering the capabilities of ViT-based models in capturing local features (Chen et al., 2024). Additionally, the attention mechanism has a high computational cost in high-resolution images, and medical images are predominantly 3D volumetric data with high resolutions, leading to a high computational complexity of volumetric medical image segmentation models (Lin et al., 2023).

To tackle these limitations, we propose a **Progres**sively Entangled Transformer Large Kernel (PTLK) module and a Collaboratively Entangled Transformer Large Kernel (CTLK) module to leverage the benefits of large kernel-based convolutional layers and self-attention from ViT and overcome their shortcomings. Specifically, PTLK and CTLK modules employ a Multi-head Large Kernel (MHLK) to capture multi-scale features with low computational complexity effectively. They utilize multiple convolutional layers with different large kernels to extract varying-scaled local features. Additionally, these convolutional layers are applied to different channels to avoid redundant feature extraction. Subsequently, PTLK and CTLK modules employ a Decomposed Efficient Selfattention (DESA) to adaptively model global information for channel features. This DESA is a more efficient way to calculate self-attention scores with lower computational complexity than standard self-attention. Finally, PTLK and CTLK employ an Attention Entanglement mechanism to aggregate features from MHLK and DESA, motivating the mutual enhancement between them. To improve the diversity of features, PTLK and CTLK implement this Attention Entanglement mechanism in two different ways. PTLK utilizes local features from MHLK to enhance global contextual information from DESA progressively. In contrast, CTLK utilizes local features from MHLK and global features from DESA to calibrate and enhance each other mutually.

ViTs employ the feed-forward network (FFN) or multilayer perceptron (MLP) module to introduce non-linearity to channels (Dosovitskiy et al., 2021; Xu et al., 2021; Liu et al., 2021). However, these FFN and MLP modules limit the representation abilities of ViTs in medical image segmentation. Specifically, they lack mechanisms to capture pixel-wise features and model spatial contextual information due to the employment of fully connected layers, thus lowering segmentation accuracy (Chen et al., 2023). To tackle this limitation, we propose a novel **Attention-gated Channel MLP** (AG-MLP) module to enhance its capabilities of capturing spatial information. AG-MLP employs a depthwise convolutional layer to capture spatial-wise features efficiently, and a spatial-wise attention gate to calibrate these features with global spatial information, thus improving the representation powers of the MLP module.

The U-shaped encoder-decoder architecture is widely employed in medical image segmentation networks, and it adapts either concatenation or summation to fuse upsampled features in the decoder with those skip-connected from the encoder (Cao et al., 2022; Lin et al., 2022; Azad et al., 2024). However, this design ignores the semantic gap of features between the decoder and the encoder, thus lowering segmentation accuracy (Wang et al., 2022). To tackle this limitation, we propose a Cross Entanglement Decoding (CED) block for efficient feature fusion and decoding. It employs two parallel paths. The first path employs a Progressive Feature Interaction (PFI) module for progressive feature interaction and fusion, and subsequently, a CTLK block is utilized to decode finer features. In the second path, a Collaborative Feature Interaction (CFI) module is employed for collaborative feature interaction and fusion, and a PTLK block is followed to decode fused features.

We propose a novel network for volumetric medical image segmentation, termed TransLK-Net, by incorporating these modules into a hierarchical ViT-based encoderdecoder architecture. Specifically, to leverage the scaling behavior of hierarchical ViTs, we incorporate PTLK and CTLK modules along with AG-MLP into a standard ViT block, generating PTLK and CTLK blocks, respectively. The encoder employs the PTLK and CTLK blocks for generic feature extraction, and the decoder employs the CED block for feature fusion and decoding. To demonstrate the generalizability of TransLK-Net, we evaluated it on four heterogeneous volumetric segmentation tasks: abdominal multiorgan CT segmentation, brain tumor MR segmentation, hepatic vessel tumor CT segmentation, and abdomen organ CT segmentation. It achieved superior segmentation performance with lower computational complexity compared with other state-of-the-art (SOTA) models. Our contributions are summarized as follows:

- We propose novel Progressively Entangled Transformer Large Kernel and Collaboratively Entangled Transformer Large Kernel modules to leverage the benefits of large kernel convolutions and transformer self-attention for generic local and global feature extraction.
- We propose a novel Attention-gated Channel MLP to equip MLP with the capabilities of capturing pixelwise spatial information, thus improving its representation powers for segmentation.
- We propose a Cross Entanglement Decoding block for efficient feature fusion and information decoding. It employs Progressive Feature Interaction and Collaborative Feature Interaction modules to fuse features

from the decoder and skip-connected from the encoder, avoiding semantic gaps during fusion.

We propose a novel network for volumetric medical image segmentation, termed TransLK-Net by incorporating these modules into a hierarchical ViT-based encoder-decoder architecture. It achieved superior performance with low computational complexity compared to other SOTA methods in four heterogeneous volumetric segmentation tasks.

2. Related work

2.1. Transformers in medical image segmentation

The introduction of vision transformer has revolutionized the field of medical image segmentation (Dosovitskiy et al., 2021). Various ViT-based segmentation networks have been proposed with great success. Swin UNet was the first pure ViT-based network for medical image segmentation (Cao et al., 2022). Medical Transformer utilized an axialgated attention mechanism in Transformer blocks for local and global feature representation (Valanarasu et al., 2021). DS-TransUNet employed duel Swin Transformer branches to capture features from patches at different scales (Lin et al., 2022). MISSFormer was built by incorporating Enhanced Transformer blocks and the Enhanced Transformer Context Bridge into a hierarchical encoder-decoder network (Huang et al., 2022). nnFormer was proposed as 3D Transformer network for volumetric medical image segmentation (Zhou et al., 2023). CSWin-UNet incorporated the cross-shaped window self-attention-based Transformer module into the UNet for efficient long-range dependencies modeling (Liu et al., 2024b). AgileFormer utilized spatially dynamic components to effectively capture heterogeneous features from target organs (Qiu et al., 2026).

2.2. Hybrid CNN-Transformer networks in medical image segmentation

To enhance the capabilities of segmentation models by leveraging the advantages of both CNNs and ViTs, some methods attempt to combine them by utilizing a ViT-based encoder and a CNN-based decoder. TransUNet utilized a Vision Transformer to encode tokenized feature maps for capturing global information and a CNN decoder to generate pixel-wise segmentation results (Chen et al., 2024). CoTr followed a similar design as TransUNet where a ViT encoder was employed to enhance features from the CNN encoder (Xie et al., 2021). UNETR and Swin UNETR employed a ViT and Swin ViT encoder respectively to learn hierarchical feature representations, and then these encoders were incorporated with a CNN decoder for segmentation (Hatamizadeh et al., 2022, 2021). TransFuse employed two parallel CNN and Transformer branches for information processing (Zhang et al., 2021). CTC-Net employed a ViT and CNN encoder to capture complementary features for a CNN decoder (Yuan et al., 2023). Similarly, CT-Net fused features from an asymmetric ViT encoder and a CNN encoder for global and local feature representations (Zhang et al., 2024). Large kernel convolutional layers were incorporated into ViT architectures to utilize local and global contextual information (Yang et al., 2026). Dynamic MLP Mixer network employed attention-enhanced MLP modules in ViT architecture (Yang et al., 2025c)

2.3. Channel-wise and spatial-wise attention mechanisms

Some attention mechanisms are proposed to enhance CNNs' capabilities of capturing long-range dependencies. The Squeeze and Excitation network was proposed to model inter-dependencies among global channels (Hu et al., 2018). Subsequently, an Efficient Channel Attention mechanism was designed to improve channel attention learning by employing a local cross-channel interaction strategy (Wang et al., 2020). The Squeeze and Attention network modeled spatial-wise attention by implementing convolution operations across pixels (Zhong et al., 2020). The Convolutional Block Attention Module (CBAM) captured inter-channel and inter-spatial dependencies of features sequentially, thus enhancing feature representation learning (Woo et al., 2018). Channel-wise and spatial-wise attention were combined in parallel to capture global information among channels and spatial positions (Roy et al., 2018).

3. Methods

3.1. Progressively Entangled Transformer Large Kernel

The PTLK module employs three components: Multi-head Large Kernel (MHLK), Progressive Attention Entanglement, and Decomposed Efficient Self-attention (DESA) (Figure 1A).

Multi-head Large Kernel. MHLK partitions input features $\boldsymbol{X}_{in} \in \mathbb{R}^{C \times D \times H \times W}$ into N heads as a set of subfeatures $\{\boldsymbol{X}_1, \boldsymbol{X}_2, ..., \boldsymbol{X}_N\} = \{\boldsymbol{X}_i \in \mathbb{R}^{\frac{C}{N} \times D \times H \times W} | i \in \{1, 2, ..., N\}\}$ along channels via a linear projection, where C represents the number of channels, and D, H, and W represent the depth, height, and width of volumetric images, respectively

$$\{X_1, X_2, ..., X_N\} = \text{Projection}(X_{in}). \tag{1}$$

Subsequently, N distinct depth-wise large kernel convolutional layers (DWConv $_{k_i}$) are utilized to extract features in each head separately. These convolutional layers have growing kernel sizes $k_i \in \{k_1, k_2, ..., k_N\}$, thus capturing varying-scaled features. We start from a convolution layer with the $3 \times 3 \times 3$ kernel size ($k_1 = 3$) and utilize convolutional layers whose kernel sizes gradually increase by 2 per head ($k_i = 3 + 2 * (i - 1)$). Features from each head are concatenated to generate the output features $X' \in \mathbb{R}^{C \times D \times H \times W}$:

$$\begin{split} \boldsymbol{X}_1' &= \mathrm{DWConv}_{k_1}(\boldsymbol{X}_1), \\ \boldsymbol{X}_2' &= \mathrm{DWConv}_{k_2}(\boldsymbol{X}_2), \\ \dots \\ \boldsymbol{X}_N' &= \mathrm{DWConv}_{k_N}(\boldsymbol{X}_N). \end{split} \tag{2}$$

Features $X_i' \in \mathbb{R}^{\frac{C}{N} \times D \times H \times W}$ from each head are concatenated to generate the output features $X' \in \mathbb{R}^{C \times D \times H \times W}$:

$$X' = \text{Concat}([X'_1, X'_2, ..., X'_N]).$$
 (3)

This design enables us to regulate the range of receptive fields and multi-granularity information without adjusting the number of heads. Additionally, these growing kernel sizes provide large receptive fields, thus capturing more long-range contextual information. Since different convolutional kernels are applied to different channels, rather than applying all kernels to each channel, redundant features from the same channel will not be captured.

Progressive Attention Entanglement. To entangle local features from MHLK to the following DESA, we utilize the Progressive Attention Entanglement mechanism to calibrate these local features X'. First, channel-wise attention is employed by cascading an adaptive average pooling layer (AvgPool), a linear layer, and a Sigmoid function. It models the importance of these kernels and inter-dependencies among these local features X', generating features $X'_{ch} \in \mathbb{R}^{C \times D \times H \times W}$

$$X'_{ch} = X' * Sigmoid(Linear(AvgPool(X'))).$$
 (4)

Subsequently, since DESA lacks mechanisms to learn spatial-wise representations, a spatial-wise attention is employed to enhance features X'_{ch} via spatial-wise global information, generating global information enhanced features $X'_{att} \in \mathbb{R}^{C \times D \times H \times W}$ for DESA. This spatial-wise attention mechanism cascades a channel pooling layer (ChPool), a $7 \times 7 \times 7$ convolutional layer (Conv7), and a Sigmoid function

$$X'_{att} = X'_{ch} * \text{Sigmoid}(\text{Conv7}(\text{ChPool}(X'_{ch}))).$$
 (5)

Decomposed Efficient Self-attention (DESA). DESA takes attention-entangled features X'_{att} as input to model their inter-dependencies and feature representations. A linear projection is applied to features X'_{att} to generate the value matrix $V_{att} \in \mathbb{R}^{C \times D \times H \times W}$. The same linear projection is applied to the output features X' from MHLK to generate the query matrix $Q \in \mathbb{R}^{C \times D \times H \times W}$ and the key matrix $K \in \mathbb{R}^{C \times D \times H \times W}$

$$\{\boldsymbol{Q}, \boldsymbol{K}, \boldsymbol{V}_{att}\} = \text{Projection}(\{\boldsymbol{X'}, \boldsymbol{X'}, \boldsymbol{X}_{att}'\}). \tag{6}$$

Subsequently, these projected vectors are split into N heads

$$Q = \{Q_{i} \in \mathbb{R}^{\frac{C}{N} \times D \times H \times W} | i \in \{1, 2, ..., N\} \}$$

$$= \{Q_{1}, Q_{2}, ..., Q_{N}\} \in \mathbb{R}^{N \times \frac{C}{N} \times D \times H \times W},$$

$$K = \{K_{i} \in \mathbb{R}^{\frac{C}{N} \times D \times H \times W} | i \in \{1, 2, ..., N\} \}$$

$$= \{K_{1}, K_{2}, ..., K_{N}\} \in \mathbb{R}^{N \times \frac{C}{N} \times D \times H \times W},$$

$$V_{att} = \{(V_{att})_{i} \in \mathbb{R}^{\frac{C}{N} \times D \times H \times W} | i \in \{1, 2, ..., N\} \}$$

$$= \{(V_{att})_{1}, (V_{att})_{2}, ..., (V_{att})_{N} \} \in \mathbb{R}^{N \times \frac{C}{N} \times D \times H \times W}.$$
(7)

The self-attention score for *i*-th head is calculated as

$$(\boldsymbol{X}_{out})_i = \operatorname{Softmax}\left(\frac{Q_i K_i^T}{\sqrt{d_m}}\right) (V_{att})_i.$$
 (8)

where $d_m = \frac{C}{N}$. However, applying this self-attention mechanism to 4D input matrices leads to high computational complexity. To avoid high complexity, we introduce an efficient way to calculate self-attention scores by decomposing 4D matrices into lower dimensions. After decomposition, it calculates attention scores between Q and K along three dimensions, H, W, and D, separately

$$(\boldsymbol{X}_{H})_{i} = \operatorname{Softmax}\left(\frac{(Q_{H})_{i}(K_{H})_{i}^{T}}{\sqrt{d_{m}}}\right)(V_{att})_{i},$$

$$(\boldsymbol{X}_{W})_{i} = \operatorname{Softmax}\left(\frac{(Q_{W})_{i}(K_{W})_{i}^{T}}{\sqrt{d_{m}}}\right)(V_{att})_{i}, \tag{9}$$

$$(\boldsymbol{X}_{out})_{i} = \operatorname{Softmax}\left(\frac{(Q_{D})_{i}(K_{D})_{i}^{T}}{\sqrt{d_{m}}}\right)(V_{att})_{i}.$$

After features from all heads are concatenated and reshaped, the output features $X_{out} \in \mathbb{R}^{C \times D \times H \times W}$ are obtained via the linear projection and the drop-out operation. Finally, a residual connection is applied

$$\mathbf{X}_{out} = \text{Concat}([(\mathbf{X}_{out})_1, (\mathbf{X}_{out})_2, ..., (\mathbf{X}_{out})_N]),
\mathbf{X}_{out} = \text{Dropout}(\text{Projection}(\mathbf{X}_{out})).$$
(10)

The final stage of PTLK applies a residual connection

$$X_{out} = X_{out} + X_{in}. (11)$$

3.2. Collaboratively Entangled Transformer Large Kernel

The CTLK module employs three components: Multihead Large Kernel, Decomposed Efficient Self-attention, and Collaborative Attention Entanglement (Figure 1B).

Multi-head Large Kernel. MHLK in CTLK shares the same design as that in PTLK. The output features $\boldsymbol{X}_{LK} \in \mathbb{R}^{C \times D \times H \times W}$ are captured from input features \boldsymbol{X}_{in} via the multiple convolutional layers with growing large kernel sizes along different channels

$$X_{LK} = MHLK(X_{in}). (12)$$

Decomposed Efficient Self-attention. DESA in CTLK has the same design as that in PTLK. The linear projection is applied to the input features \boldsymbol{X}_{in} to generate the query matrix $\boldsymbol{Q} \in \mathbb{R}^{C \times D \times H \times W}$, the key matrix $\boldsymbol{K} \in \mathbb{R}^{C \times D \times H \times W}$, and the value matrix $\boldsymbol{V} \in \mathbb{R}^{C \times D \times H \times W}$,

$$\{Q, K, V\} = \text{Projection}(\{X_{in}, X_{in}, X_{in}\}). \tag{13}$$

Subsequently, these projected vectors are split into N heads

$$\begin{aligned} & Q = \{Q_1, Q_2, ..., Q_N\}, \\ & K = \{K_1, K_2, ..., K_N\}, \\ & V = \{V_1, V_2, ..., V_N\}. \end{aligned} \tag{14}$$

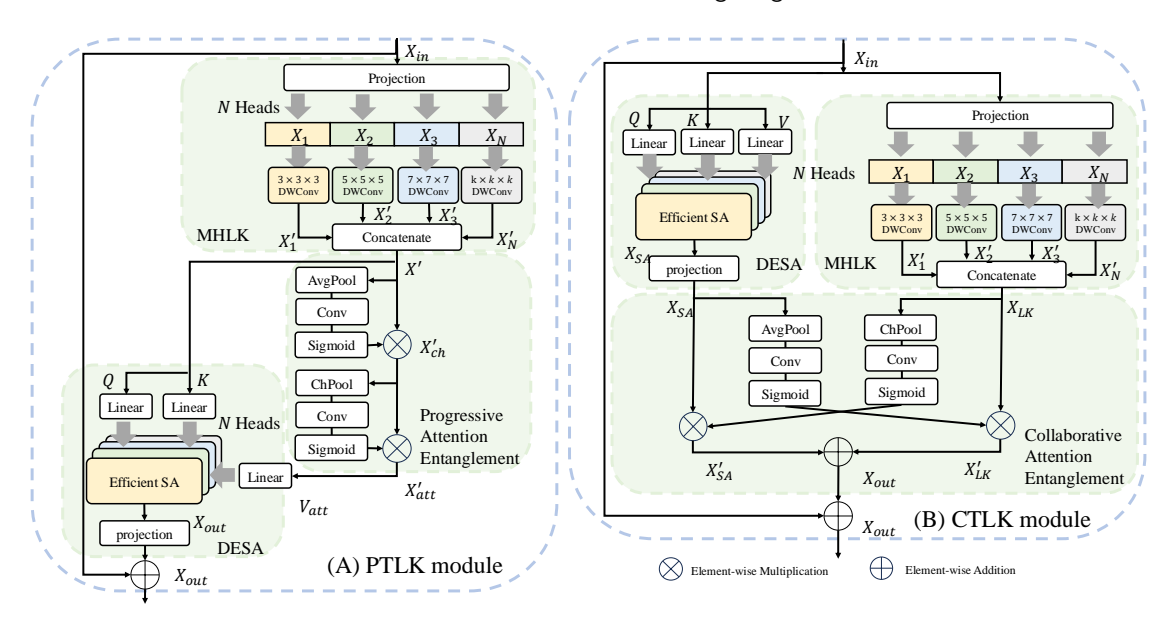


Figure 1: The architecture of the (A) PTLK module and the (B) CTLK module. (A) In PTLK, MHLK projects the input features X_{in} into N heads as sub-features $\{X_1, X_2, ..., X_N\}$ along channels. N depth-wise large kernel convolutional layers (DWConv) are utilized to capture features $\{X_1', X_2', ..., X_N'\}$. These features are concatenated as features X', and Progressive Attention Entanglement is employed to enhance X', generating features X'_{att} . DESA employs the linear projection to generate Q and K from X' and V from X'_{att} . After they are split into N heads, the efficient self-attention (SA) mechanism is employed to calculate their attention scores, generating the output features X_{out} . Lastly, a residual connection is applied to X_{in} and X_{out} . (B) In CTLK, MHLK projects the input features X_{in} into N heads as sub-features $\{X_1, X_2, ..., X_N\}$ along channels. N depth-wise large kernel convolutional layers are utilized to capture features $\{X_1', X_2', ..., X_N'\}$. These features are concatenated as features X_{LK} . DESA employs the linear projection to create Q, K, and V with N heads from features X_{in} . The efficient self-attention mechanism is employed to calculate their attention scores, generating the output features X_{SA} . Subsequently, the Collaborative Attention Entanglement is employed to enhance features X_{LK} and X_{SA} , generating features X'_{LK} and X'_{SA} . Lastly, they are added to generate output features X_{out} , and a residual connection is applied to X_{in} and X_{out}

The self-attention scores are calculated efficiently in the same way

$$(\boldsymbol{X}_{W})_{i} = \operatorname{Softmax}\left(\frac{(Q_{W})_{i}(K_{W})_{i}^{T}}{\sqrt{d_{m}}}\right)V_{i},$$

$$(\boldsymbol{X}_{H})_{i} = \operatorname{Softmax}\left(\frac{(Q_{H})_{i}(K_{H})_{i}^{T}}{\sqrt{d_{m}}}\right)V_{i},$$

$$(\boldsymbol{X}_{SA})_{i} = \operatorname{Softmax}\left(\frac{(Q_{D})_{i}(K_{D})_{i}^{T}}{\sqrt{d_{m}}}\right)V_{i}.$$
(15)

After features from all heads are concatenated, the output features $X_{SA} \in \mathbb{R}^{C \times D \times H \times W}$ are obtained via the linear projection and the drop-out operation

$$\boldsymbol{X}_{SA} = \text{Concat}([(\boldsymbol{X}_{SA})_1, (\boldsymbol{X}_{SA})_2, ..., (\boldsymbol{X}_{SA})_N]),$$

 $\boldsymbol{X}_{SA} = \text{Dropout}(\text{Projection}(\boldsymbol{X}_{SA})).$ (16)

Collaborative Attention Entanglement. Collaborative Attention Entanglement employs channel-wise and spatial-wise attention to improve mutual calibration between local features from MHLK and global features from DESA, thus improving representation capabilities collaboratively. Specifically, MHLK captures varying-scaled spatial local features, while DESA lacks mechanisms to capture spatial-wise localization information. Thus, spatial-wise attention

maps are extracted from local features of MHLK X_{LK} to demonstrate the important spatial contextual information. These spatial-wise attention maps are utilized to calibrate features from DESA X_{SA} , enhancing their spatial representations. This spatial-wise attention is implemented by cascading a channel pooling layer, a $7 \times 7 \times 7$ convolutional layer, and a Sigmoid function

$$X'_{SA} = X_{SA} * \text{Sigmoid}(\text{Conv7}(\text{ChPool}(X_{LK}))).$$
(17)

In contrast, DESA captures channel-wise global information, while MHLK lacks abilities to capture this information due to the limitation of convolutional kernels. Thus, channel-wise attention maps are extracted from output features of DESA \boldsymbol{X}_{SA} to model inter-dependencies among channels. These channel-wise attention maps are utilized to calibrate features from MHLK \boldsymbol{X}_{LK} , improving them with channel-wise global information. This channel-wise attention is implemented by cascading an adaptive average pooling layer, a linear layer, and a Sigmoid function.

$$X'_{LK} = X_{LK} * \text{Sigmoid}(\text{Linear}(\text{AvgPool}(X_{SA})))$$
(18)

Finally, these two calibrated features are fused via addition as the output features $\pmb{X}_{out} \in \mathbb{R}^{C \times D \times H \times W}$. A residual

connection is applied

$$X_{out} = X'_{LK} + X'_{SA},$$

$$X_{out} = X_{out} + X_{in}.$$
(19)

3.3. Attention-gated Channel MLP module

We propose an Attention-gated Channel MLP (AGMLP) module by introducing a spatial-wise attention gate into the channel MLP module (Figure 2F). Specifically, given the input features $\boldsymbol{X}_{in} \in \mathbb{R}^{C \times D \times H \times W}$, a linear projection layer is employed to expand channels by 4 as features $\boldsymbol{X} \in \mathbb{R}^{4C \times D \times H \times W}$ and a GELU function is applied to introduce non-linearity

$$X = GELU(Projection(X_{in})).$$
 (20)

Subsequently, a $3 \times 3 \times 3$ depth-wise convolutional layer is employed to extract local spatial features $\boldsymbol{X}_{sp} \in \mathbb{R}^{4C \times D \times H \times W}$

$$X_{sp} = DWConv(X). (21)$$

Additionally, a spatial-wise attention gate employs a $1 \times 1 \times 1$ convolutional layer $(Conv_1)$ to capture spatial-wise global information and a Sigmoid function to convert them to attention-gating scores $\mathbf{A} \in \mathbb{R}^{4C \times D \times H \times W}$

$$\mathbf{A} = \operatorname{Sigmoid}(\operatorname{Conv}_{1}(\mathbf{X})). \tag{22}$$

Subsequently, features X_{sp} are adjusted by these attentiongating scores to improve their capabilities of learning spatial representations

$$X = X_{sp} * A. (23)$$

A second linear projection layer is employed to compress channels to the original dimension as $X_{out} \in \mathbb{R}^{C \times D \times H \times W}$. Two drop-out layers are employed before and after it

$$X_{out} = \text{Dropout}(\text{Projection}(\text{Dropout}(X))).$$
 (24)

3.4. Entangled Transformer Large Kernel block

The Progressively Entangled Transformer Large Kernel block (PTLK $_B$) is constructed by using the PTLK module and AG-MLP to replace self-attention and MLP in a standard hierarchical ViT block, respectively (Figure 2B). Two Layer Normalization (LN) layers are employed before PTLK and AG-MLP. A residual connection is also applied to each module. The output of the l-th layer in PTLK $_B$ can be computed as

$$\mathbf{X}^{l} = \text{PTLK}(\text{LN}(\mathbf{X}^{l-1})) + \mathbf{X}^{l-1},$$

$$\hat{\mathbf{X}}^{l} = \text{AG-MLP}(\text{LN}(\mathbf{X}^{l})) + \mathbf{X}^{l}.$$
(25)

The Collaboratively Entangled Transformer Large Kernel block (CTLK $_B$) is constructed in the same way as PTLK $_B$ (Figure 2B). The output of the l-th layer in CTLK $_B$ can be computed as

$$X^{l} = \operatorname{CTLK}(\operatorname{LN}(X^{l-1})) + X^{l-1},$$

$$\hat{X}^{l} = \operatorname{AG-MLP}(\operatorname{LN}(X^{l})) + X^{l}.$$
(26)

3.5. Cross Entanglement Decoding block

The CED block employs a dual-path architecture (Figure 2C). Specifically, the first path employs a Progressive Feature Interaction (PFI) module to fuse skip-connected features from the encoder $\boldsymbol{X}_{skip} \in \mathbb{R}^{C \times D \times H \times W}$ and upsampled features in the decoder $\boldsymbol{X}_{up} \in \mathbb{R}^{C \times D \times H \times W}$, generating features $\boldsymbol{X}_1 \in \mathbb{R}^{C \times D \times H \times W}$. Subsequently, a CTLK_B is applied to decode more contextual information from $\boldsymbol{X}_1 \in \mathbb{R}^{C \times D \times H \times W}$ as $\hat{\boldsymbol{X}}_1 \in \mathbb{R}^{C \times D \times H \times W}$

$$\mathbf{X}_{1} = PFI(\mathbf{X}_{skip}; \mathbf{X}_{up}),
\hat{\mathbf{X}}_{1} = CTLK_{B}(\mathbf{X}_{1}).$$
(27)

Another path employs a Collaborative Feature Interaction (CFI) module to fuse features \boldsymbol{X}_{skip} and \boldsymbol{X}_{up} , generating features $\boldsymbol{X}_2 \in \mathbb{R}^{C \times D \times H \times W}$. Subsequently, a PTLK_B is applied to decode more contextual information from $\boldsymbol{X}_2 \in \mathbb{R}^{C \times D \times H \times W}$ as $\hat{\boldsymbol{X}}_2 \in \mathbb{R}^{C \times D \times H \times W}$

$$\begin{aligned} \boldsymbol{X}_2 &= \mathrm{CFI}(\boldsymbol{X}_{skip}; \boldsymbol{X}_{up}), \\ \hat{\boldsymbol{X}}_2 &= \mathrm{PTLK}_{R}(\boldsymbol{X}_2). \end{aligned} \tag{28}$$

Lastly, output features of the CED block $m{X}_{out} \in \mathbb{R}^{C \times D \times H \times W}$ are generated by adding features $\hat{m{X}}_1$ and $\hat{m{X}}_2$

$$\boldsymbol{X}_{out} = \hat{\boldsymbol{X}}_1 + \hat{\boldsymbol{X}}_2. \tag{29}$$

3.5.1. Progressive Feature Interaction module

In the PFI module (Figure 2D), features \boldsymbol{X}_{skip} are split along channels to generate \boldsymbol{X}_{skip}^1 and \boldsymbol{X}_{skip}^2 , and \boldsymbol{X}_{up} are also split to generate \boldsymbol{X}_{up}^1 and \boldsymbol{X}_{up}^2 ($\boldsymbol{X}_{skip}^1, \boldsymbol{X}_{skip}^2, \boldsymbol{X}_{up}^1, \boldsymbol{X}_{up}^2 \in \mathbb{R}^{\frac{C}{2} \times D \times H \times W}$). These sub-features are cross-grouped as $\boldsymbol{X}^1 \in \mathbb{R}^{C \times D \times H \times W}$ and $\boldsymbol{X}^2 \in \mathbb{R}^{C \times D \times H \times W}$ via concatenation

$$\begin{split} \boldsymbol{X}^{1} &= \operatorname{Concat}([\boldsymbol{X}_{skip}^{1}, \boldsymbol{X}_{up}^{1}]), \\ \boldsymbol{X}^{2} &= \operatorname{Concat}([\boldsymbol{X}_{skip}^{2}, \boldsymbol{X}_{up}^{2}]). \end{split} \tag{30}$$

Subsequently, the interactions between features X^1 and X^2 are explored using MHLK, DESA, and Progressive Attention Entanglement. Specifically, MHLK is employed to extract finer spatial features $X^{1'}$ from X^1 , and the Progressive Attention Entanglement is utilized to enhance $X^{1'}$. Lastly, after projecting $X^{1'}$ to V_{att} and X^2 to Q and K, DESA is applied to model correlations between $X^{1'}$ and X^2 to generate the output features X_1 of PFI.

3.5.2. Collaborative Feature Interaction module

In the CFI module (Figure 2E), we utilize the same strategy to split features X_{skip} and X_{up} and cross-group them to X^1 and X^2 as PFI. Subsequently, the interactions between features X^1 and X^2 are explored using MHLK, DESA, and Collaborative Attention Entanglement. Specifically, MHLK is employed to extract finer spatial local features $X^{1'}$ from X^1 , and DESA is employed to capture global channel features $X^{2'}$ from X^2 . Then Collaborative Attention Entanglement is employed to improve mutual calibration between $X^{1'}$ and $X^{2'}$ and fuse them, generating output features X_2 of CFI.

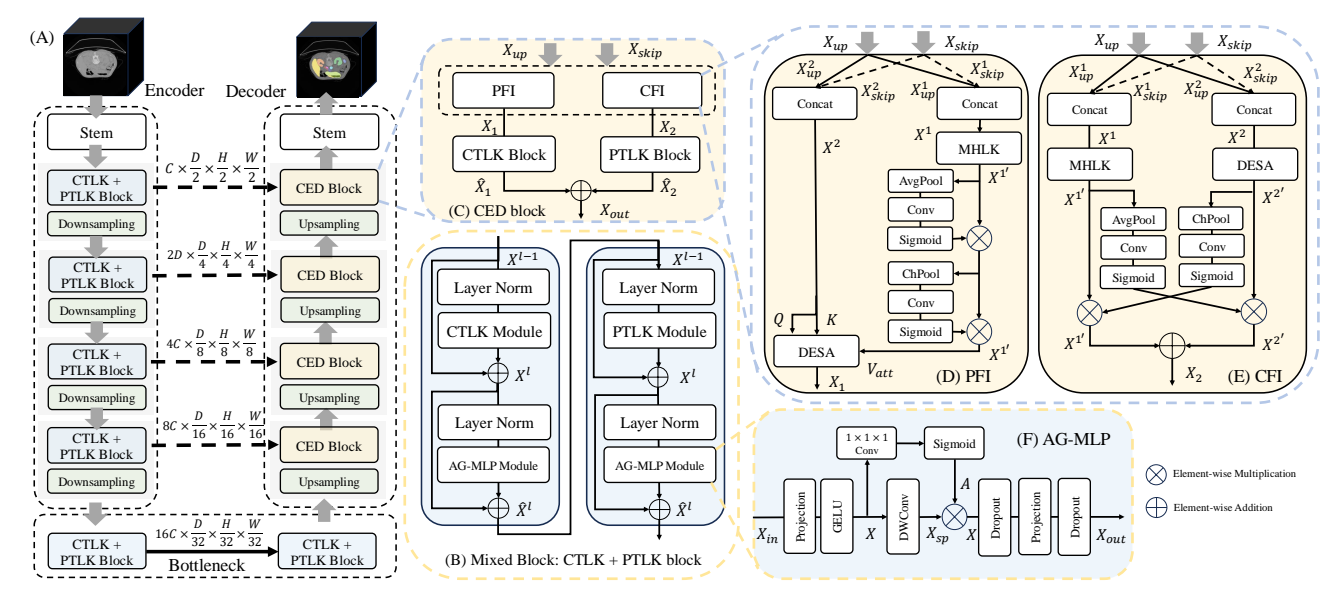


Figure 2: The architecture of (A) TransLK-Net, (B) mixed block (CTLK+PTLK block), (C) CED block, (D) PFI module, (E) CFI module, and (F) AG-MLP module. (A) TransLK-Net consists of an encoder, a bottleneck, and a decoder. The encoder and the bottleneck employ a mixed block at each stage, and the decoder employs a CED block at each stage. (B) The mixed block is built by stacking a CTLK and PTLK block. Each CTLK and PTLK block employs a CTLK and PTLK module, respectively, and both of them employ an AG-MLP module. (C) The CED block employs two parallel paths to fuse features X_{up} and X_{skip} and generate X_1 and X_2 in the PFI and CFI module. Each path employs a CTLK and PTLK block to generate features \hat{X}_1 and \hat{X}_2 , and they are added as output X_{out} . (D) the PFI module splits upsampled features X_{up} to X_{up}^1 and X_{up}^2 and skip-connected features X_{skip} to X_{skip}^1 and X_{skip}^2 . These sub-features are cross-grouped as X^1 and X^2 . Subsequently, features $X^{1'}$ are extracted from X^1 in MHLK and enhanced with Progressive Attention Entanglement. DESA takes X_2 and $X^{1'}$ as input to generate output features X_1 . (E) the CFI module employs the same strategy to generate X_1 and X_2 from X_{up} and X_{skip} . Features X_1 and X_2 in MHLK and DESA, and subsequently enhanced with Collaborative Attention Entanglement as output X_2 . (F) the AG-MLP module projects input features X_{in} to X_1 , and employs a depth-wise convolutional layer to capture spatial-wise features X_{sp} . Attention-gating scores X_1 are extracted from X_1 and used to calibrate spatial features X_{sp} . Features are projected back to output X_{out} .

3.6. Architecture of TransLK-Net

The TransLK-Net is designed as an encoder-decoder architecture to learn hierarchical feature representations (Figure 2). Both encoder and decoder comprise four stages, each with downsampling and upsampling rates of 2, 4, 8, and 16, respectively. A bottleneck is utilized to bridge the encoder and the decoder.

Encoder. The stem employs a convolutional layer with a large $7 \times 7 \times 7$ kernel and a stride of 2 to partition the input image with the dimension of $D \times H \times W$ into overlapping feature embedding. Instead of extracting the non-overlapped patches by linear projections, this design allows the model to capture richer local features from input images (Wu et al., 2021). Moreover, employing the large kernel provides a large receptive field, thus capturing more informative features and improving segmentation performance. Additionally, this stem projects features to C-dimensional vectors (C = 48) to generate features with the dimensions of $C \times \frac{D}{2} \times \frac{H}{2} \times \frac{W}{2}$. At each stage, a CTLK block and a PTLK block are stacked as a mixed block for generic feature extraction. Subsequently, a $3 \times 3 \times 3$ convolution layer with a stride of 2 is employed for downsampling. It is utilized to increase the dimension of token features and downsample the feature maps by a factor

of 2. The number of feature maps at each stage is 96, 192, 384, and 768, respectively.

Bottleneck. The bottleneck stacks a CTLK and PTLK block to extract features without changing their dimensions.

Decoder. A $2 \times 2 \times 2$ transposed convolutional layer with a stride of 2 is employed at each stage. It upsamples feature maps from the last stage by decreasing their channel numbers and upscaling their dimensions by a factor of 2. Subsequently, the CED block is employed to fuse upsampled features with skip-connected features from the encoder, decoding richer contextual information. To recover the feature maps to the original dimension $D \times H \times W$, the stem employs a $2 \times 2 \times 2$ transposed convolutional layer with a stride of 2. Lastly, a $1 \times 1 \times 1$ convolutional layer is used to produce the voxel-wise predictions for segmentation.

4. Experiments

4.1. Datasets

We implemented our experiments on four segmentation tasks to evaluate the superiority of our segmentation networks. These tasks differ in image modalities, segmentation complexity, number of structures to be segmented, and spatial and phenotypic heterogeneity (Table 1). They are designed to underline the potential of TransLK-Net to generalize across different segmentation tasks.

Abdominal Multi-organ Segmentation. We implemented abdominal multi-organ segmentation on the MIC-CAI 2022 AMOS Challenge dataset (Ji et al., 2022). It consists of 300 abdominal CT images with voxel-level annotations of 15 organs (Spleen, Right kidney, Left kidney, Gall bladder, Esophagus, Liver, Stomach, Aorta, Postcava, Pancreas, Right Adrenal Gland, Left Adrenal Gland, Duodenum, Bladder, and Prostate). Each CT volume consists of 67 ~ 369 slices of 512 × 512 pixels with a slice spacing of 1.25 ~ 5.00 mm.

Brain Tumor Segmentation. The Brain Tumor segmentation dataset is from the Medical Segmentation Decathlon (MSD) Challenge (Antonelli et al., 2022). It comprises 484 multi-parametric Magnetic Resonance Imaging (MRI) scans with three foreground segmentation labels, including Edema (ED), Enhancing Tumor (ET), and Non-Enhancing Tumor (NET). Four modalities are available for each case: Native T1-weighted image (T1w), post-contrast T1-weighted (T1Gd), T2-weighted (T2w), and T2 Fluid Attenuated Inversion Recovery (T2-FLAIR).

Hepatic Vessel Tumor Segmentation. The MSD Hepatic Vessel Tumor segmentation dataset consists of 303 CT scans with manual annotations (Antonelli et al., 2022). The target segmentation regions are the hepatic vessels (Vessel) and tumors within the liver (Tumor). They are obtained from patients with a variety of primary and metastatic liver tumors.

Abdomen CT Organ Segmentation. The fourth dataset is from The Fast and Low GPU memory Abdominal oRgan sEgmentation (FLARE) challenge (Ma et al., 2022). It consists of 361 CT images with voxel-wise annotations of four abdominal organs, including the liver, the kidneys, the spleen, and the pancreas. It demonstrates a large diversity across various centers, vendors, phases, and diseases.

4.2. Implementation details

The experiments were implemented using PyTorch. Models were trained and validated on NVIDIA Tesla A100 PCI-E Passive Single GPU each with 40GB of GDDR5 memory. We used a joint loss function (\mathcal{L}_{Total}) that consists of cross-entropy loss (\mathcal{L}_{CE}) and dice loss (\mathcal{L}_{Dice})

$$\mathcal{L}_{Total} = \mathcal{L}_{CE}(\hat{y}, y) + \mathcal{L}_{Dice}(\hat{y}, y)$$
 (31)

where y and \hat{y} denote the ground truth annotations and predictions. Implementation details were customized for different segmentation tasks (Table 1).

We employed the 5-fold cross-validation to generate reliable evaluation results on all datasets. Segmentation performance was evaluated by the Dice Similarity Coefficient (DSC). The architecture complexity was evaluated by the

 Table 1

 Dataset information and implementation details.

Dataset	AMOS 2022	Brain Tumor	Hepatic Vessel	l FLARE		
Dataset	AIVIOS 2022	Brain Tumor	nepatic vessei	FLARE		
Tasks	Multi-Organs	Tissues	Tubular&Tumor	Multi-Organs		
Modalities	CT	MR	CT	CT		
Dimensions	3D	3D	3D	3D		
Class Number	15	3	2	4		
Batch size	2	2	2	2		
Patch size	96 × 160 × 160	$128 \times 128 \times 128$	64 × 192 × 192	96 × 192 × 160		
Preprocessing	[5%, 95%] clipping. Z score normalization					
Epochs	1500					
Optimizer		Ada	mW			
Ir schedule		cos	sine			
Initial Ir (TransLK-Net)	5e-3	5e-5	1e-3	1e-3		
Decay rate (TransLK-Net)	3e-5	3e-6	3e-5	3e-5		
		Rotation: (-30, 30)	with 0.2 probability	y		
		Scaling: (0.7, 1.4)	with 0.2 probability	,		
Augmentation	Mirroring: 0.5 probability					
Augmentation	Gaussian noise, Gaussian blurring: 0.15 probability					
			rast: 0.15 probabili			
	(Samma transformat	ion: 0.15 probabilit	y		

number of parameters (Params), and the computational complexity was evaluated by the number of Floating Point Operations (FLOPs). The Wilcoxon signed-rank test was implemented to statistically quantify the differences in segmentation performance between TransLK-Net and SOTA methods.

4.3. Comparison of with State-of-the-arts

We compared the performance of TransLK-Net with various SOTA 3D volumetric segmentation models for a thoughtful comparison. These methods include

- CNN-based methods: VNet (Milletari et al., 2016), nnU-Net (Isensee et al., 2021), Attention gated U-Net (Att U-Net) (Oktay et al., 2018)
- ViT-based methods: nnFormer (Zhou et al., 2023), SegFormer (Perera et al., 2024)
- Hybrid CNN-ViT-based methods: TransBTS (Wang et al., 2021b), UNETR (Hatamizadeh et al., 2022), Swin UNETR (Hatamizadeh et al., 2021), 3D UX Net (Lee et al., 2023), MedNeXt (Roy et al., 2023), VSmTrans (Liu et al., 2024a) and MixUNETR (Shen et al., 2025)

4.3.1. Comparison of TransLK-Net with State-of-the-arts

AMOS Multi-organ segmentation. TransLK-Net achieved the best and most robust segmentation performance in multi-organ segmentation from CT, demonstrating the highest mean DSC score of 89.76 and the lowest standard deviation of 11.68 than other SOTA methods (Table 2 and Figure 3). Specifically, TransLK-Net achieved superior segmentation performance than CNN-based methods while maintaining much lower computational complexity. Att U-Net and nnU-Net achieved better performance than other methods, but TransLK-Net demonstrated 2.69 and 2.71 higher points in DSC scores with 69% and 67% fewer Params and 319% and 314% fewer FLOPs, respectively. Additionally, TransLK-Net demonstrated much higher segmentation performance than ViT-based methods. Although SegFormer

Table 2 Comparison of segmentation performance among TransLK-Net and SOTA methods on the 2022 AMOS Abdominal Multi-organ segmentation task. The performance was evaluated using the DSC (%; Mean \pm Standard Deviation). **Bold** represents the best results. (*: p < 0.01 with Wilcoxon signed-rank test between TransLK-Net and SOTA methods.)

Tasks	VNet	nnU-Net	Att U-Net	TransBTS	UNETR	Swin UNETR	nnFormer	SegFormer	UX-Net	MedNeXt	VSmTrans	MixUNETR	TransLK-Net
Spleen	95.07±8.49	96.14±8.29	96.06±8.26	95.81±8.28	92.34±10.65	95.77±8.38	95.18±8.28	91.82±10.54	95.98±8.34	95.82±8.30	95.84±8.32	95.04±8.81	97.58±2.01
R. kidney	94.82±7.60	95.54±7.99	95.79±5.81	95.51±5.74	92.10±10.95	95.19±8.25	94.02±6.05	92.31±6.77	95.28±8.32	95.48±5.79	95.44±6.18	94.41±9.22	96.86±1.38
L. kidney	94.69±8.58	95.44±9.38	95.47±8.79	94.85±10.18	91.33±13.52	95.00±9.88	93.79±9.59	91.30±11.44	94.92±10.63	94.92±8.64	94.65±11.38	94.29±10.05	96.64±7.54
Gall bladder	76.78±25.79	81.62±23.68	82.07±23.50	81.83±21.95	67.46±27.89	79.94±25.10	81.23±21.06	69.55±26.09	80.36±24.63	79.53±25.35	81.62±23.71	78.36±24.90	84.96±21.38
Esophagus	79.29±10.88	83.72±9.28	83.44±9.77	81.95±10.04	74.32±13.68	82.75±9.91	78.74±11.30	68.29±13.31	83.14±9.97	81.41±11.14	83.24±9.49	79.69±10.69	86.24±8.64
Liver	96.66±2.30	97.44±1.82	97.37±1.98	97.20±2.06	95.04±4.20	97.14±2.38	96.73±2.59	95.41±3.22	97.20±2.55	97.16±2.29	97.25±2.19	96.65±3.17	97.58±1.80
Stomach	87.09±16.32	90.38±15.37	90.23±15.59	89.25±15.73	79.17±18.70	88.53±16.68	88.95±15.35	82.36±16.92	88.72±16.88	88.99±16.20	89.85±15.66	87.44±16.78	92.50±15.02
Aorta	91.10±6.74	93.74±5.15	93.53±5.37	92.85±5.82	89.89±6.27	93.89±5.32	90.85±7.51	89.89±4.38	93.77±5.30	90.39±7.43	94.92±3.21	94.13±3.87	96.05±2.58
Postcava	85.42±8.93	89.34±6.59	89.02±6.98	87.17±9.17	81.93±8.24	88.95±6.35	83.13±13.30	82.80±6.98	88.95±6.84	86.00±11.02	89.99±5.63	88.53±5.95	91.64±5.81
Pancreas	80.37±12.61	84.20±11.81	84.22±12.01	82.13±12.74	73.38±16.00	82.74±13.46	78.73±14.28	74.32±14.29	83.54±13.11	82.50±13.28	84.13±11.92	81.48±13.53	86.97±8.74
R.A. gland	72.44±13.03	74.81±14.45	74.69±14.02	73.36±13.92	68.22±14.94	75.32±13.04	69.08±14.00	58.38±11.51	75.69±13.48	74.12±14.29	74.99±12.57	72.87±12.58	79.12±7.56
L.A. gland	73.35±14.66	75.20±14.97	75.43±14.68	73.83±15.46	65.68±18.02	75.30±15.09	69.62±14.20	54.59±14.36	75.84±14.89	74.59±14.94	75.81±14.21	72.59±15.05	80.96±7.88
Duodenum	73.42±14.97	78.94±14.54	78.72±14.81	76.46±16.11	65.05±15.58	77.45±14.79	72.40±16.41	67.19±14.19	77.92±15.27	76.48±15.95	79.52±14.31	75.52±14.86	82.94±10.24
Bladder	83.32±19.07	87.68±15.95	87.89±15.50	87.31±14.64	75.94±21.69	86.75±16.10	85.74±15.41	77.83±18.46	86.83±17.74	86.59±16.01	87.51±15.45	84.36±18.20	90.48±12.28
Prostate	78.30±19.04	82.23±20.56	82.20±19.48	82.12±18.72	73.71±21.09	81.04±19.67	80.74±18.64	74.67±19.51	81.13±20.84	80.92±19.49	80.95±20.86	78.96±19.78	86.32±18.08
Mean	84.14±16.18	87.10±15.16	87.08±14.95	86.11±15.23	79.04±18.99	86.38±15.48	83.93±16.09	78.05±18.74	86.62±15.65	85.66±15.82	87.05±14.96	84.96±16.06	89.79*±11.46

Table 3 Comparison of segmentation performance among TransLK-Net and SOTA methods on the Brain Tumor segmentation, Hepatic Vessel Tumor segmentation, and FLARE Abdomen Organ segmentation. The performance was evaluated using the DSC (%; Mean \pm Standard Deviation). Bold represents the best results. (*: p < 0.01 with Wilcoxon signed-rank test between TransLK-Net and SOTA methods.)

Tasks	Brain Tumor Segmentation			Hepatic Vessel Tumor Segmentation			FLARE Abdomen Organ segmentation					
Methods	Mean	ET	ED	NET	Mean	Vessel	Tumor	Mean	Liver	Kidney	Spleen	Pancreas
V-Net	72.55±21.97	77.08±22.96	79.33±13.08	61.28±23.59	64.30±21.76	62.44±12.41	66.16±28.03	93.54±8.40	98.24±1.07	96.07±3.50	98.04±1.40	81.84±9.00
nnU-Net	73.50±21.44	78.79±21.48	80.33±12.23	61.37±23.38	65.38±21.16	63.45±12.54	67.31±27.04	94.38±7.50	98.53±0.81	96.61±3.22	98.29±1.04	84.11±8.36
Att U-Net	73.43±21.48	78.56±21.69	80.38±11.97	61.35±23.45	65.91±21.20	62.77±12.54	69.05±26.87	94.43±7.37	98.53±0.77	96.63±3.02	98.26±0.93	84.32±8.25
TransBTS	73.80±21.17	78.87±21.64	80.78 ± 11.60	61.74±22.84	64.94±21.11	61.76±12.17	68.13±26.89	93.96±8.32	98.44±1.03	96.43±3.71	98.19±1.84	82.78 ± 9.45
UNETR	72.56±21.70	78.00±22.04	79.73±11.65	59.94±23.48	57.24±24.49	61.80±12.36	52.67±31.70	92.19±10.61	97.87±1.78	95.99±3.25	96.95±6.79	77.96±10.89
Swin UNETR	73.52±21.36	78.53±21.72	80.49±11.92	61.55±23.20	62.63±22.62	61.95±12.61	63.32±29.39	93.78±8.48	98.35±1.56	96.47±3.52	97.95±3.70	82.36±9.13
nnFormer	73.52±21.31	78.64±21.57	80.37±12.06	61.60±23.16	66.06±20.30	62.61±12.10	69.51±25.57	93.81±7.77	98.29±1.00	95.97±2.35	97.93±1.46	83.05±8.67
SegFormer	46.00±26.41	40.20±26.66	63.84±17.25	33.95±24.26	58.73±21.97	54.37±10.32	63.10±28.64	92.58±8.99	97.90±0.98	95.23±3.14	96.98±5.29	80.22±8.77
UX Net	60.86±22.78	64.90±24.74	66.65±15.37	51.04±23.75	63.49±21.65	62.65±12.41	64.33±27.96	93.84±8.54	98.41±1.29	96.46±3.94	98.21±1.42	82.30±9.59
MedNeXt	73.86±21.29	79.14±21.32	80.70±11.64	61.73±23.40	66.01±20.61	62.54±12.58	69.49±25.82	94.11±7.75	98.40±1.11	96.44±3.50	98.17±1.28	83.45±8.42
VSmTrans	73.98±21.30	79.22±21.47	80.77±11.83	61.94±23.28	64.88±20.60	62.05±12.81	67.71±25.86	94.18±7.62	98.41±1.20	96.49 ± 3.50	98.20±1.59	83.65±8.14
MixUNETR	74.08±20.85	79.06±21.75	80.67±11.53	62.55 ± 22.30	62.64±21.42	62.47±12.29	62.81 ± 27.69	93.94±8.03	98.37±1.19	96.49±3.35	98.08±1.92	82.82±8.63
TransLK-Net	74.73*±19.86	80.13±20.89	81.42±9.31	62.64 ±22.18	67.89*±20.12	64.91 ±10.66	70.87 ±26.04	94.83*±6.04	98.60±1.03	97.17 ±1.27	98.33 ±0.88	85.22 ± 5.17

Table 4 Comparison of model complexity among TransLK-Net and SOTA methods. Params and FLOPs were evaluated using input patches with dimensions of $96\times96\times96$.

Methods	Params (M)	FLOPs (G)
VNet	45.66	370.52
Att U-Net	69.08	360.98
nnU-Net	68.38	357.13
TransBTS	31.58	110.69
UNETR	92.78	82.73
Swin UNETR	62.19	329.28
nnFormer	149.33	284.28
SegFormer	4.50	5.02
UX Net	53.01	632.33
MedNeXt	11.65	178.05
VSmTrans	50.39	358.21
MixUNETR	62.03	329.99
TransLK-Net	40.95	86.17

presented lower complexity, TransLK-Net achieved 11.74 higher points in DSC score. TransLK-Net outperformed hybrid CNN-ViT methods. VSmTrans demonstrated the highest DSC score among hybrid CNN-ViT methods, but TransLK-Net achieved 2.74 higher DSC points with 23%

fewer Params and 316% fewer FLOPs. Although MedNeXt and TransBTS demonstrated fewer Params, TransLK-Net achieved 4.13 and 3.68 higher DSC points with 107% and 28% fewer FLOPs than them. Additionally, TransLK-Net demonstrated much better segmentation performance than SOTA methods in organs with heterogeneous shapes and sizes, such as adrenal glands, pancreas, duodenum, and aorta. Thus, TransLK-Net has superior capabilities of capturing varying-scaled features from multiple organs.

Brain Tumor segmentation. TransLK-Net demonstrated superior segmentation performance than SOTA methods in brain tumor segmentation from MR imaging, achieving 74.73 points in the mean DSC score (Table 3 and Figure 3). Specifically, MixUNETR demonstrated better performance than other SOTA methods in this task, but TransLK outperformed it by 0.65 points in DSC with 51% fewer Params and 283% fewer FLOPs. nnU-Net achieved the better segmentation performance than other CNN-based methods, but TransLK-Net outperformed it by 1.23 points. nnFormer was initially designed to advance brain tumor segmentation in MR images, but TransLK-Net achieved 1.21 higher points in DSC with 265% fewer Params and 230% fewer FLOPs. Compared to Swin UNETR which was proposed as a hybrid CNN-ViT method for brain tumor

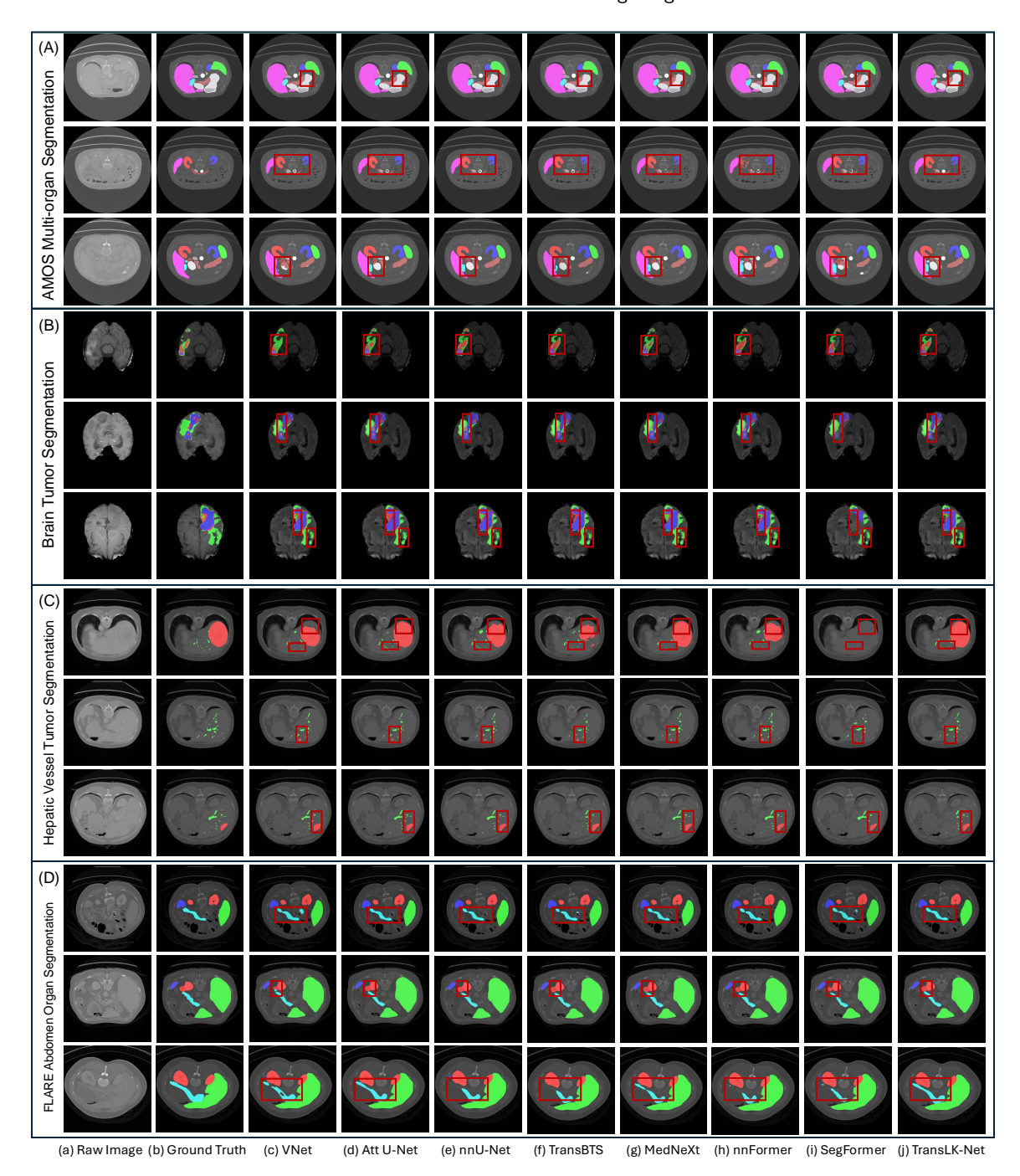


Figure 3: Qualitative comparison between (j) TransLK-Net and (a) Raw image, (b) ground truth, (c) VNet, (d) Att U-Net, (e) nnU-Net, (f) TransBTS, (g) MedNeXt, (h) nnFormer, and (i) SegFormer. Results are shown across four public datasets, including (A) the AMOS 2022 Multi-organ dataset, (B) the MSD Brain Tumor dataset, (C) the MSD Hepatic Vessel Tumor dataset, and (D) the FLARE Abdomen Organ dataset. Red boxes mark the regions where TransLK-Net demonstrates higher segmentation quality than other methods.

segmentation, but TransLK-Net achieved 1.21 higher points in DSC with 52% fewer Params and 282% fewer FLOPs.

Hepatic Vessel Tumor segmentation. TransLK-Net achieved the highest DSC scores of 67.89 with the lowest standard deviation of 20.12 among various methods, demonstrating superior and robust performance in this hepatic vessel and tumor segmentation task (Table 3 and Figure

3). Specifically, compared with Att U-Net which demonstrated better performance than other CNN-based methods, TransLK-Net achieved approximately 2 higher points in DSC. nnFormer achieved the best performance among SOTA methods, but TransLK-Net outperformed it by 1.83 DSC points. Among various hybrid CNN-ViT methods, MedNeXt showed the best performance, but TransLK-Net

demonstrated 1.88 higher DSC points. UX Net employs large kernel-based convolutions in hybrid CNN-ViT architecture to capture features by large receptive fields, but TransLK-Net achieved 4.4 higher points while employing 29% fewer Params and 634% fewer FLOPs. Additionally, TransLK-Net achieved the highest DSC points among various methods in vessel and tumor segmentation tasks. Thus, TransLK-Net presented superior capabilities for capturing features from tubular structures and heterogeneous tissues.

FLARE Abdomen Organ segmentation. In this diverse abdominal organ segmentation task, TransLK-Net demonstrated superior segmentation performance, achieving the highest 94.83 DSC points and the lowest 6.04 standard deviation (Table 3 and Figure 3). Specifically, Att U-Net and nnU-Net achieved better segmentation results than other SOTA methods, but TransLK-Net demonstrated 0.4 and 0.45 higher DSC points than them, respectively. TransLK-Net achieved approximately 1 – 2.4 higher DSC scores than ViT-based methods. Additionally, TransLK-Net demonstrated 0.72 and 0.65 higher DSC scores than two hybrid CNN-ViT methods, MedNext and VSmTrans.

4.4. Ablation studies

We implemented ablation studies on PTLK and CTLK blocks, the CED block, the AG-MLP module, and the optimal head number to investigate their impact on segmentation performance and computational complexity.

We constructed TransLK-ViT from TransLK-Net for easily implementing ablation studies. Instead of the decoder in the TransLK-Net, TransLK-ViT employed a ViT-based decoder which was symmetric to its encoder. Specifically, a CTLK block and a PTLK block were stacked and incorporated into each decoder stage. Features skip-connected from the encoder \boldsymbol{X}_{skip} and features upsampled from the last stage \boldsymbol{X}_{up} were concatenated along channels. Subsequently, a $1 \times 1 \times 1$ convolutional layer was employed to recover the channel number. This fusion strategy was commonly utilized in U-shaped encoder-decoder segmentation models.

We implemented TransLK-NETR by incorporating PTLK and CTLK blocks into a widely used hybrid CNN-ViT architecture (Figure 5). This architecture is employed in several volumetric segmentation methods, such as UNETR (Hatamizadeh et al., 2021), Swin UNETR (Hatamizadeh et al., 2021), UX Net (Lee et al., 2023), VSmTrans (Liu et al., 2024a), and MixUNETR (Shen et al., 2025). These networks utilize the same CNN-based decoder, but they incorporate different blocks into the ViT-based encoder. In the TransLK-NETR, the encoder stacks a CTLK and PTLK block as a mixed block at each stage.

4.4.1. Analysis of Entanglement Transformer Large Kernel block

To investigate the impact of the CTLK and PTLK blocks, we incorporated different blocks into TransLK-ViT and TransLK-NETR. The mixed blocks (CTLK+PTLK) were originally incorporated into each stage of these networks. Subsequently, two MHLK blocks (MHLK+MHLK), two DESA blocks (DESA+DESA), two PTLK blocks (PTLK+PTLK),

Table 5

Comparison of segmentation performance and computational complexity among different basic modules in TransLK-ViT and TransLK-NETR on 2022 AMOS Multi-organ segmentation task. Performance was evaluated using DSC (%; Mean \pm STD). The Params and FLOPs were evaluated using input patches with dimensions of $96 \times 96 \times 96$.

Backbones	Blocks	DSC	Params (M)	FLOPs (G)
	MHLK + MHLK	87.78±14.90	34.61	66.32
	DESA + DESA	87.93±14.66	35.84	71.18
TransLK-ViT	PTLK + PTLK	88.66±13.95	38.55	78.07
	CTLK + CTLK	88.62±14.17	40.51	78.05
	CTLK + PTLK	89.06±13.86	39.53	78.06
	MHLK + MHLK	88.61±13.74	45.29	338.77
	DESA + DESA	88.67±13.66	45.45	341.15
TransLK-NETR	PTLK + PTLK	89.04±13.24	46.08	344.58
	CTLK + CTLK	88.92±13.18	46.47	344.57
	CTLK + PTLK	89.32±12.46	46.28	344.57

or two CTLK blocks (CTLK+CTLK) were incorporated, separately.

TransLK-ViT achieved the highest DSC scores of 89.06 when the mixed block (CTLK+PTLK) was incorporated into the encoder and the decoder (Table 6 and Figure 4). Specifically, incorporating this mixed block into TransLK-ViT achieved superior performance than incorporating two sub-components, two MHLK or DESA blocks, with a slight increase in Params and FLOPs. Additionally, employing the mixed block achieved 0.4 and 0.44 higher DSC scores than employing a uniform block, two PTLK or CTLK blocks, respectively, with relatively the same computational complexity.

When TransLK-NETR was incorporated the mixed block (CTLK+PTLK), it achieved the highest DSC scores of 89.32 (Table 5 and Figure 4). Incorporation of the mixed block into TransLK-NETR outperformed the incorporation of two MHLK or two DESA blocks, and two PTLK or CTLK blocks.

Employing PTLK and CTLK blocks improved the segmentation performance over employing separate large kernel convolution or self-attention modules. Additionally, PTLK and CTLK blocks utilized different mechanisms to entangle features from MHLK and DESA, so employing the mixed block enhanced the network's capabilities to capture diverse features, thus improving segmentation performance compared with employing the uniform block.

4.4.2. Comparison of Entanglement Transformer Large Kernel block with other blocks

We compared TransLK-NETR with UNETR, Swin UNETR, UX Net, VSmTrans, and MixUNETR to demonstrate the superior performance of PTLK and CTLK blocks over other blocks. TransLK-NETR demonstrated superior segmentation performance than those hybrid CNN-ViT methods in all four segmentation tasks (Table 6 and Figure 6). These results demonstrate the superior capabilities of our PTLK and CTLK blocks over other large kernel and

Table 6 Comparison of segmentation performance among TransLK-NETR and other methods on the four tasks. The performance was evaluated using the DSC (%; Mean \pm Standard Deviation). **Bold** represents the best results. The Params and FLOPs were evaluated using the input patches with the dimension of $96 \times 96 \times 96$. (*: p < 0.01 with Wilcoxon signed-rank test between TransLK-NETR and SOTA methods.)

Networks	AMOS 2022	Brain Tumor	Hepatic Vessel Tumor	FLARE	Params (M)	FLOPs (G)
UNETR	79.04±18.99	72.56±21.70	57.24±24.49	92.19±10.61	92.78	82.73
Swin UNETR	86.38±15.48	73.52±21.36	62.63±22.62	93.78 <u>±</u> 8.48	62.19	329.28
UX-Net	86.62±15.65	60.86±22.78	63.49 <u>±</u> 21.65	93.84 <u>±</u> 8.54	53.01	632.33
VSmTrans	87.05±14.96	73.98±21.30	64.88±20.60	94.18±7.62	50.39	358.21
MixUNETR	84.96±16.06	74.08±20.85	62.64±21.42	93.94±8.03	62.03	329.99
TransLK-NETR	89.32 *±12.46	74.43 *±19.90	67.61 *±20.06	94.75 *±6.38	46.28	344.57

transformer blocks. Specifically, UNETR and Swin UN-ETR employ ViT and Swin ViT blocks for feature encoding, respectively, but TransLK-NETR achieved 10.28 and 2.94 higher points in DSC with 100% and 34% fewer Params than them in AMOS multi-organ segmentation, respectively. UX Net employs large kernel-based convolutions, but TransLK-NETR outperformed it by 2.7 higher points in DSC while utilizing 15% fewer Params and 84% fewer FLOPs. VSmTrans and MixUNETR employ hybrid convolution-ViT blocks to encode features. TransLK-NETR achieved superior segmentation performance over them by 2.27 and 4.36 higher points in DSC. Additionally, TransLK-NETR utilized approximately 9% fewer Params and 4% fewer FLOPs than VSmTrans, and 51% fewer Params than MixUNETR. TransLK-NETR also demonstrated the best performance in the brain tumor segmentation, hepatic vessel tumor segmentation, and abdomen CT organ segmentation tasks.

4.4.3. Analysis of Cross Entanglement Decoding block

To evaluate the impact of the CED block, we compared the segmentation performance and computational complexity of TransLK-Net with TransLK-ViT in four tasks. This study was designed to compare the performance of the CED block in TransLK-Net with the common ViT-based decoding block in TransLK-ViT.

TransLK-Net achieved higher segmentation performance than TransLK-ViT in four tasks, demonstrating the superiority of the CED block over standard fusion strategies in U-shaped methods (Table 7). Specifically, TransLK-Net achieved 0.73 and 0.39 higher points in DSC than TransLK-ViT in AMOS and FLARE abdominal multi-organ segmentation tasks, while slightly increasing around 3.6% Params and 10% FLOPs. TransLK-Net demonstrated 0.58 higher points in DSC than TransLK-ViT in brain tumor segmentation. When segmenting the hepatic vessel and tumor, TransLK-Net and TransLK-ViT achieved competitive performance.

4.4.4. Ablation Study on AG-MLP

To demonstrate the improvement of AG-MLP on segmentation performance over the FFN and standard MLP, we

Table 7 Comparison of segmentation performance and computational complexity between TransLK-ViT and TransLK-Net on four segmentation tasks. Performance was evaluated using DSC (%; Mean \pm STD). The Params and FLOPs were evaluated using input patches with dimensions of $96 \times 96 \times 96$.

Tasks	TransLK-ViT	TransLK-Net
AMOS Multi-organ	89.06±13.86	89.79±11.46
Brain Tumor	74.15±21.51	74.73±19.86
Vessel Tumor	67.80±19.74	67.89±20.12
FLARE Abdomen Organ	94.44±6.87	94.83±6.04
Params (M)	39.53	40.95
FLOPs (G)	78.06	86.17

Table 8 Comparison of segmentation performance and computational complexity between AG-MLP and FFN, MLP in TransLK-Net on 2022 AMOS Multi-organ segmentation task. Performance was evaluated using DSC (%; Mean \pm STD). The Params and FLOPs were evaluated using the input patches with the dimension of $96\times96\times96$.

Modules	DSC	Params (M)	FLOPs (G)
FFN	88.22±13.66	38.94	73.31
MLP	88.59±12.15	40.86	85.63
AG-MLP	89.79 <u>±</u> 11.46	40.95	86.17

implemented an ablation study on AG-MLP in TransLK-Net. Employing AG-MLP in TransLK-Net improved segmentation performance with a slight increase in computational complexity compared with FFN and MLP (Table 8 and Figure 7). Specifically, incorporating AG-MLP into TransLK-Net achieved 1.57 and 1.2 higher points in DSC with 5.2% and 0.2% more Params and 17.5% and 0.6% more FLOPs than incorporating FFN and MLP, respectively. Thus, the employment of AG-MLP improves the segmentation performance of these networks by enhancing their capabilities of learning spatial representations.

Table 9

Comparison of segmentation performance and computational complexity among TransLK-Net employing different head numbers N on 2022 AMOS Multi-organ segmentation task. Performance was evaluated using DSC (%; Mean \pm STD). The Params (M) and FLOPs (G) were evaluated using the input patches with the dimension of $96 \times 96 \times 96$.

Head N	Mean DSC	Params (M)	FLOPs (G)
2	87.51±12.96	40.43	82.32
3	89.79±11.46	40.95	86.19
4	87.51±12.96 89.79±11.46 89.54±11.86	41.78	92.27

4.4.5. Analysis of the Optimal Head Number

PTLK and CTLK blocks employ a hyper-parameter. termed the head number N, in MHLK and DESA. It describes how channels are split and how convolutional layers and self-attention are applied. Specifically, splitting channels into multiple heads enables MHLK to apply different convolutional layers to avoid redundant feature extraction. MHLK will grow the kernel size k with N as k = 3 + 2 *(N-1) to capture multi-scale features. Similarly, calculating self-attention scores in multiple heads ensures DESA focuses on different parts of input sequences, thus capturing richer features. To investigate its impact on segmentation performance and find the optimal value, we evaluated the performance of TransLK-Net when it employed different N. Specifically, we set the minimal number of N as 2 to leverage the benefits of splitting channels to multiple heads. In contrast, splitting channels with a large head number leads to high computational complexity and difficulty in network optimization. Additionally, this N should be set to make sure channels can be equally divided. Therefore, we investigated three potential numbers for N (N = 2, 3, and 4) (Table 9).

Employing three heads (N = 3) in TransLK-Net demonstrated the best segmentation performance, improving DSC scores by 2.28 points than employing two heads (N = 2), while slightly increasing 1.39% Params and 4.7% FLOPs, respectively. Employing convolution layers with more varying kernels enhanced models' capabilities of capturing more diverse features, thus improving segmentation performance. Additionally, employing convolutions with larger kernels slightly increased the computational complexity of these networks since these convolutions are applied within each head to avoid redundant feature extraction. Moreover, employing three heads in TransLK-Net achieved competitive performance with employing four heads (N = 4) with fewer Params and FLOPs. Thus, we selected 3 as the optimal head number N^* and split channels to three heads in MHLK and DESA.

5. Conclusion

We propose a novel TransLK-Net for volumetric medical image segmentation by leveraging the benefits of large kernel convolutions and transformer self-attention to encode and decode features progressively and collaboratively. It

employs the Progressively Entangled Transformer Large Kernel module and the Collaboratively Entangled Transformer Large Kernel module to capture mutually-calibrated local and global features. Subsequently, the Cross Entanglement Decoding block is built based on these two modules to enhance feature interactions and fusion. Additionally, AG-MLP is proposed to improve the capabilities of FFN and MLP in spatial feature learning. We evaluated TransLK-Net on four heterogeneous segmentation tasks, and it demonstrated superior segmentation performance with lower computation complexity compared to various SOTA methods. Due to their high generalizability and applicability, we believe that TransLK-Net has the potential to achieve promising segmentation performance on various medical image segmentation tasks.

Declaration of competing interests

The authors declare that they have no known competing financial interests or personal relationships that could have appeared to influence the work reported in this paper.

Acknowledgments

Computations were performed using the facilities of the Washington University Research Computing and Informatics Facility (RCIF). The RCIF has received funding from NIH S10 program grants: 1S10OD025200-01A1 and 1S10OD030477-01.

CRediT authorship contribution statement

JY: conceptualization, methodology, formal analysis, writing the original draft, reviewing, and editing, visualization; DM: methodology, writing, reviewing, and editing, supervision; AS: methodology, writing, reviewing, and editing, supervision.

References

Alam, M.S., Wang, D., Liao, Q., Sowmya, A., 2022. A multi-scale context aware attention model for medical image segmentation. IEEE Journal of Biomedical and Health Informatics 27, 3731–3739.

Antonelli, M., Reinke, A., Bakas, S., Farahani, K., Kopp-Schneider, A., Landman, B.A., Litjens, G., Menze, B., Ronneberger, O., Summers, R.M., et al., 2022. The medical segmentation decathlon. Nature communications 13, 4128.

Aslani, S., Dayan, M., Storelli, L., Filippi, M., Murino, V., Rocca, M.A., Sona, D., 2019. Multi-branch convolutional neural network for multiple sclerosis lesion segmentation. NeuroImage 196, 1–15.

Azad, R., Niggemeier, L., Hüttemann, M., Kazerouni, A., Aghdam, E.K., Velichko, Y., Bagci, U., Merhof, D., 2024. Beyond self-attention: Deformable large kernel attention for medical image segmentation, in: Proceedings of the IEEE/CVF Winter Conference on Applications of Computer Vision, pp. 1287–1297.

Bello, I., Zoph, B., Vaswani, A., Shlens, J., Le, Q.V., 2019. Attention augmented convolutional networks, in: Proceedings of the IEEE/CVF international conference on computer vision, pp. 3286–3295.

Bullock, J., Cuesta-Lázaro, C., Quera-Bofarull, A., 2019. Xnet: a convolutional neural network (cnn) implementation for medical x-ray image segmentation suitable for small datasets, in: Medical Imaging 2019:

- Biomedical Applications in Molecular, Structural, and Functional Imaging, SPIE. pp. 453–463.
- Cai, Z., Fan, Q., Feris, R.S., Vasconcelos, N., 2016. A unified multi-scale deep convolutional neural network for fast object detection, in: Computer Vision–ECCV 2016: 14th European Conference, Amsterdam, The Netherlands, October 11–14, 2016, Proceedings, Part IV 14, Springer. pp. 354–370.
- Cao, H., Wang, Y., Chen, J., Jiang, D., Zhang, X., Tian, Q., Wang, M., 2022. Swin-unet: Unet-like pure transformer for medical image segmentation, in: European conference on computer vision, Springer. pp. 205–218.
- Chen, G., Dai, Y., Zhang, J., Yin, X., Cui, L., 2022. Mbanet: Multi-branch aware network for kidney ultrasound images segmentation. Computers in biology and medicine 141, 105140.
- Chen, J., Mei, J., Li, X., Lu, Y., Yu, Q., Wei, Q., Luo, X., Xie, Y., Adeli, E., Wang, Y., et al., 2024. Transunet: Rethinking the u-net architecture design for medical image segmentation through the lens of transformers. Medical Image Analysis, 103280.
- Chen, Z., Zhang, Y., Gu, J., Kong, L., Yang, X., Yu, F., 2023. Dual aggregation transformer for image super-resolution, in: Proceedings of the IEEE/CVF international conference on computer vision, pp. 12312– 12321.
- Dosovitskiy, A., Beyer, L., Kolesnikov, A., Weissenborn, D., Zhai, X., Unterthiner, T., Dehghani, M., Minderer, M., Heigold, G., Gelly, S., Uszkoreit, J., Houlsby, N., 2021. An image is worth 16x16 words: Transformers for image recognition at scale, in: International Conference on Learning Representations. URL: https://openreview.net/forum?id=YicbFdNTTy.
- Fan, Q., Huang, H., Chen, M., Liu, H., He, R., 2024. Rmt: Retentive networks meet vision transformers, in: Proceedings of the IEEE/CVF Conference on Computer Vision and Pattern Recognition, pp. 5641– 5651.
- Fu, Y., Mazur, T.R., Wu, X., Liu, S., Chang, X., Lu, Y., Li, H.H., Kim, H., Roach, M.C., Henke, L., et al., 2018. A novel mri segmentation method using cnn-based correction network for mri-guided adaptive radiotherapy. Medical physics 45, 5129–5137.
- Hatamizadeh, A., Nath, V., Tang, Y., Yang, D., Roth, H.R., Xu, D., 2021. Swin unetr: Swin transformers for semantic segmentation of brain tumors in mri images, in: International MICCAI Brainlesion Workshop, Springer. pp. 272–284.
- Hatamizadeh, A., Tang, Y., Nath, V., Yang, D., Myronenko, A., Landman, B., Roth, H.R., Xu, D., 2022. Unetr: Transformers for 3d medical image segmentation, in: Proceedings of the IEEE/CVF winter conference on applications of computer vision, pp. 574–584.
- Hu, J., Shen, L., Sun, G., 2018. Squeeze-and-excitation networks, in: Proceedings of the IEEE conference on computer vision and pattern recognition, pp. 7132–7141.
- Huang, H., Lin, L., Tong, R., Hu, H., Zhang, Q., Iwamoto, Y., Han, X., Chen, Y.W., Wu, J., 2020. Unet 3+: A full-scale connected unet for medical image segmentation, in: ICASSP 2020-2020 IEEE international conference on acoustics, speech and signal processing (ICASSP), IEEE. pp. 1055–1059.
- Huang, X., Deng, Z., Li, D., Yuan, X., Fu, Y., 2022. Missformer: An effective transformer for 2d medical image segmentation. IEEE Transactions on Medical Imaging 42, 1484–1494.
- Isensee, F., Jaeger, P.F., Kohl, S.A., Petersen, J., Maier-Hein, K.H., 2021. nnu-net: a self-configuring method for deep learning-based biomedical image segmentation. Nature methods 18, 203–211.
- Ji, Y., Bai, H., Ge, C., Yang, J., Zhu, Y., Zhang, R., Li, Z., Zhanng, L., Ma, W., Wan, X., et al., 2022. Amos: A large-scale abdominal multiorgan benchmark for versatile medical image segmentation. Advances in neural information processing systems 35, 36722–36732.
- Khadangi, A., Boudier, T., Rajagopal, V., 2021. Em-stellar: benchmarking deep learning for electron microscopy image segmentation. Bioinformatics 37, 97–106
- Kónya, S., Natarajan, T.S., Allouch, H., Nahleh, K.A., Dogheim, O.Y., Boehm, H., 2021. Convolutional neural network-based automated segmentation and labeling of the lumbar spine x-ray. Journal of Craniovertebral Junction and Spine 12, 136–143.

- Lee, H.H., Bao, S., Huo, Y., Landman, B.A., 2023. 3d UX-net: A large kernel volumetric convnet modernizing hierarchical transformer for medical image segmentation, in: The Eleventh International Conference on Learning Representations. URL: https://openreview.net/forum?id=ws7si0SvtRA
- Lin, A., Chen, B., Xu, J., Zhang, Z., Lu, G., Zhang, D., 2022. Ds-transunet: Dual swin transformer u-net for medical image segmentation. IEEE Transactions on Instrumentation and Measurement 71, 1–15.
- Lin, T.Y., Dollár, P., Girshick, R., He, K., Hariharan, B., Belongie, S., 2017.
 Feature pyramid networks for object detection, in: Proceedings of the IEEE conference on computer vision and pattern recognition, pp. 2117–2125.
- Lin, W., Wu, Z., Chen, J., Huang, J., Jin, L., 2023. Scale-aware modulation meet transformer, in: Proceedings of the IEEE/CVF International Conference on Computer Vision, pp. 6015–6026.
- Liu, T., Bai, Q., Torigian, D.A., Tong, Y., Udupa, J.K., 2024a. Vsmtrans: A hybrid paradigm integrating self-attention and convolution for 3d medical image segmentation. Medical Image Analysis, 103295.
- Liu, X., Gao, P., Yu, T., Wang, F., Yuan, R.Y., 2024b. Cswin-unet: Transformer unet with cross-shaped windows for medical image segmentation. Information Fusion, 102634.
- Liu, Z., Lin, Y., Cao, Y., Hu, H., Wei, Y., Zhang, Z., Lin, S., Guo, B., 2021. Swin transformer: Hierarchical vision transformer using shifted windows, in: Proceedings of the IEEE/CVF international conference on computer vision, pp. 10012–10022.
- Ma, J., Zhang, Y., Gu, S., An, X., Wang, Z., Ge, C., Wang, C., Zhang, F., Wang, Y., Xu, Y., et al., 2022. Fast and low-gpu-memory abdomen ct organ segmentation: the flare challenge. Medical Image Analysis 82, 102616.
- Milletari, F., Navab, N., Ahmadi, S.A., 2016. V-net: Fully convolutional neural networks for volumetric medical image segmentation, in: 2016 fourth international conference on 3D vision (3DV), Ieee. pp. 565–571.
- Minnema, J., van Eijnatten, M., Kouw, W., Diblen, F., Mendrik, A., Wolff, J., 2018. Ct image segmentation of bone for medical additive manufacturing using a convolutional neural network. Computers in biology and medicine 103, 130–139.
- Moeskops, P., Viergever, M.A., Mendrik, A.M., De Vries, L.S., Benders, M.J., Išgum, I., 2016. Automatic segmentation of mr brain images with a convolutional neural network. IEEE transactions on medical imaging 35, 1252–1261.
- Oktay, O., Schlemper, J., Folgoc, L.L., Lee, M., Heinrich, M., Misawa, K., Mori, K., McDonagh, S., Hammerla, N.Y., Kainz, B., Glocker, B., Rueckert, D., 2018. Attention u-net: Learning where to look for the pancreas, in: Medical Imaging with Deep Learning. URL: https://openreview.net/forum?id=Skft7cijM.
- Oztel, I., Yolcu, G., Ersoy, I., White, T., Bunyak, F., 2017. Mitochondria segmentation in electron microscopy volumes using deep convolutional neural network, in: 2017 IEEE International Conference on Bioinformatics and Biomedicine (BIBM), IEEE. pp. 1195–1200.
- Perera, S., Navard, P., Yilmaz, A., 2024. Segformer3d: an efficient transformer for 3d medical image segmentation, in: Proceedings of the IEEE/CVF Conference on Computer Vision and Pattern Recognition, pp. 4981–4988.
- Qiu, P., Yang, J., Kumar, S., Ghosh, S.S., Sotiras, A., 2026. Agileformer: Spatially agile and scalable transformer for medical image segmentation. Biomedical Signal Processing and Control 112, 108842.
- Ronneberger, O., Fischer, P., Brox, T., 2015. U-net: Convolutional networks for biomedical image segmentation, in: Medical image computing and computer-assisted intervention–MICCAI 2015: 18th international conference, Munich, Germany, October 5-9, 2015, proceedings, part III 18, Springer. pp. 234–241.
- Roy, A.G., Navab, N., Wachinger, C., 2018. Recalibrating fully convolutional networks with spatial and channel "squeeze and excitation" blocks. IEEE transactions on medical imaging 38, 540–549.
- Roy, S., Koehler, G., Ulrich, C., Baumgartner, M., Petersen, J., Isensee, F., Jaeger, P.F., Maier-Hein, K.H., 2023. Mednext: transformer-driven scaling of convnets for medical image segmentation, in: International

- Conference on Medical Image Computing and Computer-Assisted Intervention, Springer. pp. 405–415.
- Schlemper, J., Oktay, O., Schaap, M., Heinrich, M., Kainz, B., Glocker, B., Rueckert, D., 2019. Attention gated networks: Learning to leverage salient regions in medical images. Medical image analysis 53, 197–207.
- Seferbekov, S., Iglovikov, V., Buslaev, A., Shvets, A., 2018. Feature pyramid network for multi-class land segmentation, in: Proceedings of the IEEE conference on computer vision and pattern recognition workshops, pp. 272–275.
- Shen, Q., Zheng, B., Li, W., Shi, X., Luo, K., Yao, Y., Li, X., Lv, S., Tao, J., Wei, Q., 2025. Mixunetr: A u-shaped network based on w-msa and depth-wise convolution with channel and spatial interactions for zonal prostate segmentation in mri. Neural Networks 181, 106782.
- Valanarasu, J.M.J., Oza, P., Hacihaliloglu, I., Patel, V.M., 2021. Medical transformer: Gated axial-attention for medical image segmentation, in: Medical image computing and computer assisted intervention–MICCAI 2021: 24th international conference, Strasbourg, France, September 27– October 1, 2021, proceedings, part I 24, Springer. pp. 36–46.
- Wang, H., Cao, P., Wang, J., Zaiane, O.R., 2022. Uctransnet: rethinking the skip connections in u-net from a channel-wise perspective with transformer, in: Proceedings of the AAAI conference on artificial intelligence, pp. 2441–2449.
- Wang, Q., Wu, B., Zhu, P., Li, P., Zuo, W., Hu, Q., 2020. Eca-net: Efficient channel attention for deep convolutional neural networks, in: Proceedings of the IEEE/CVF conference on computer vision and pattern recognition, pp. 11534–11542.
- Wang, S., Li, C., Wang, R., Liu, Z., Wang, M., Tan, H., Wu, Y., Liu, X., Sun, H., Yang, R., et al., 2021a. Annotation-efficient deep learning for automatic medical image segmentation. Nature communications 12, 5015
- Wang, W., Chen, C., Ding, M., Yu, H., Zha, S., Li, J., 2021b. Transbts: Multimodal brain tumor segmentation using transformer, in: Medical Image Computing and Computer Assisted Intervention–MICCAI 2021: 24th International Conference, Strasbourg, France, September 27–October 1, 2021, Proceedings, Part I 24, Springer. pp. 109–119.
- Woo, S., Park, J., Lee, J.Y., Kweon, I.S., 2018. Cbam: Convolutional block attention module, in: Proceedings of the European conference on computer vision (ECCV), pp. 3–19.
- Wu, H., Xiao, B., Codella, N., Liu, M., Dai, X., Yuan, L., Zhang, L., 2021.
 Cvt: Introducing convolutions to vision transformers, in: Proceedings of the IEEE/CVF international conference on computer vision, pp. 22–31.
- Xie, Y., Zhang, J., Shen, C., Xia, Y., 2021. Cotr: Efficiently bridging cnn and transformer for 3d medical image segmentation, in: Medical Image Computing and Computer Assisted Intervention–MICCAI 2021: 24th International Conference, Strasbourg, France, September 27–October 1, 2021, Proceedings, Part III 24, Springer, pp. 171–180.
- Xu, W., Xu, Y., Chang, T., Tu, Z., 2021. Co-scale conv-attentional image transformers, in: Proceedings of the IEEE/CVF international conference on computer vision, pp. 9981–9990.
- Yang, J., Marcus, D.S., Sotiras, A., 2023. Abdominal ct pancreas segmentation using multi-scale convolution with aggregated transformations, in: Medical Imaging 2023: Computer-Aided Diagnosis, SPIE. pp. 416–424.
- Yang, J., Marcus, D.S., Sotiras, A., 2025a. Dmc-net: Lightweight dynamic multi-scale and multi-resolution convolution network for pancreas segmentation in ct images. Biomedical Signal Processing and Control 109, 107896.
- Yang, J., Marcus, D.S., Sotiras, A., 2025b. Dynamic u-net: Adaptively calibrate features for abdominal multiorgan segmentation, in: Medical Imaging 2025: Computer-Aided Diagnosis, SPIE. pp. 326–334.
- Yang, J., Qiu, P., Zhang, Y., Marcus, D.S., Sotiras, A., 2026. D-net: Dynamic large kernel with dynamic feature fusion for volumetric medical image segmentation. Biomedical Signal Processing and Control 113, 108837.
- Yang, J., Yang, J., Yu, X., Qiu, P., Prajapat, S., 2025c. D2-mlp: Dynamic decomposed mlp mixer for medical image segmentation, in: ICASSP 2025-2025 IEEE International Conference on Acoustics, Speech and Signal Processing (ICASSP), IEEE. pp. 1–5.

- Yang, J., Yu, X., Qiu, P., Marcus, D., Sotiras, A., 2025d. Active source-free cross-domain and cross-modality adaptation for volumetric medical image segmentation by image sensitivity and organ heterogeneity sampling, in: International Conference on Medical Image Computing and Computer-Assisted Intervention, Springer. pp. 3–12.
- Yin, Y., Han, Z., Jian, M., Wang, G.G., Chen, L., Wang, R., 2023. Amsunet: A neural network using atrous multi-scale convolution for medical image segmentation. Computers in Biology and Medicine 162, 107120.
- Yuan, F., Zhang, Z., Fang, Z., 2023. An effective cnn and transformer complementary network for medical image segmentation. Pattern Recognition 136, 109228.
- Zhang, N., Yu, L., Zhang, D., Wu, W., Tian, S., Kang, X., Li, M., 2024.
 Ct-net: Asymmetric compound branch transformer for medical image segmentation. Neural Networks 170, 298–311.
- Zhang, Y., Liu, H., Hu, Q., 2021. Transfuse: Fusing transformers and cnns for medical image segmentation, in: Medical Image Computing and Computer Assisted Intervention–MICCAI 2021: 24th International Conference, Strasbourg, France, September 27–October 1, 2021, Proceedings, Part I 24, Springer. pp. 14–24.
- Zhao, Q., Sheng, T., Wang, Y., Tang, Z., Chen, Y., Cai, L., Ling, H., 2019. M2det: A single-shot object detector based on multi-level feature pyramid network, in: Proceedings of the AAAI conference on artificial intelligence, pp. 9259–9266.
- Zhao, X., Li, L., Lu, W., Tan, S., 2018. Tumor co-segmentation in pet/ct using multi-modality fully convolutional neural network. Physics in Medicine & Biology 64, 015011.
- Zhong, Z., Lin, Z.Q., Bidart, R., Hu, X., Daya, I.B., Li, Z., Zheng, W.S., Li, J., Wong, A., 2020. Squeeze-and-attention networks for semantic segmentation, in: Proceedings of the IEEE/CVF conference on computer vision and pattern recognition, pp. 13065–13074.
- Zhou, H.Y., Guo, J., Zhang, Y., Han, X., Yu, L., Wang, L., Yu, Y., 2023. nnformer: Volumetric medical image segmentation via a 3d transformer. IEEE Transactions on Image Processing.
- Zhou, T., Yang, J., Cui, L., Zhang, N., Chai, S., 2024. Sbc-al: Structure and boundary consistency-based active learning for medical image segmentation, in: International Conference on Medical Image Computing and Computer-Assisted Intervention, Springer. pp. 283–293.
- Zhou, Z., Rahman Siddiquee, M.M., Tajbakhsh, N., Liang, J., 2018. Unet++: A nested u-net architecture for medical image segmentation, in: Deep Learning in Medical Image Analysis and Multimodal Learning for Clinical Decision Support: 4th International Workshop, DLMIA 2018, and 8th International Workshop, ML-CDS 2018, Held in Conjunction with MICCAI 2018, Granada, Spain, September 20, 2018, Proceedings 4, Springer. pp. 3–11.

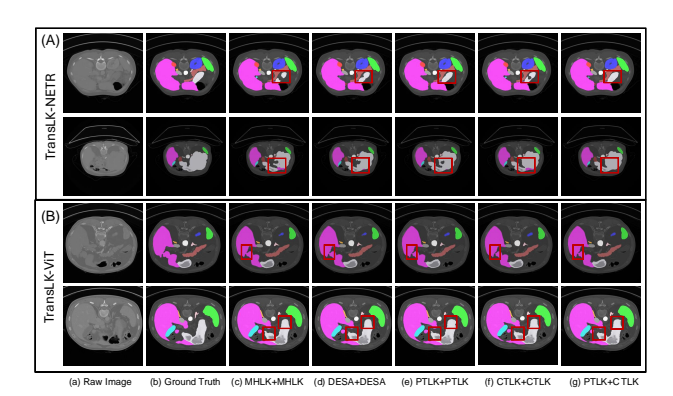


Figure 4: Qualitative comparison of (A) TransLK-NETR and (B) TransLK-ViT with their different designs on AMOS multiorgan segmentation task. They were incorporated with (c) two MHLK blocks (MHLK+MHLK), (d) two DESA blocks (DESA+DESA), (e) two PTLK blocks (PTLK+PTLK), (f) two CTLK blocks (CTLK+CTLK), and (g) the mixed blocks (CTLK+PTLK). Red boxes mark the regions where the mixed blocks demonstrate better segmentation results than others.

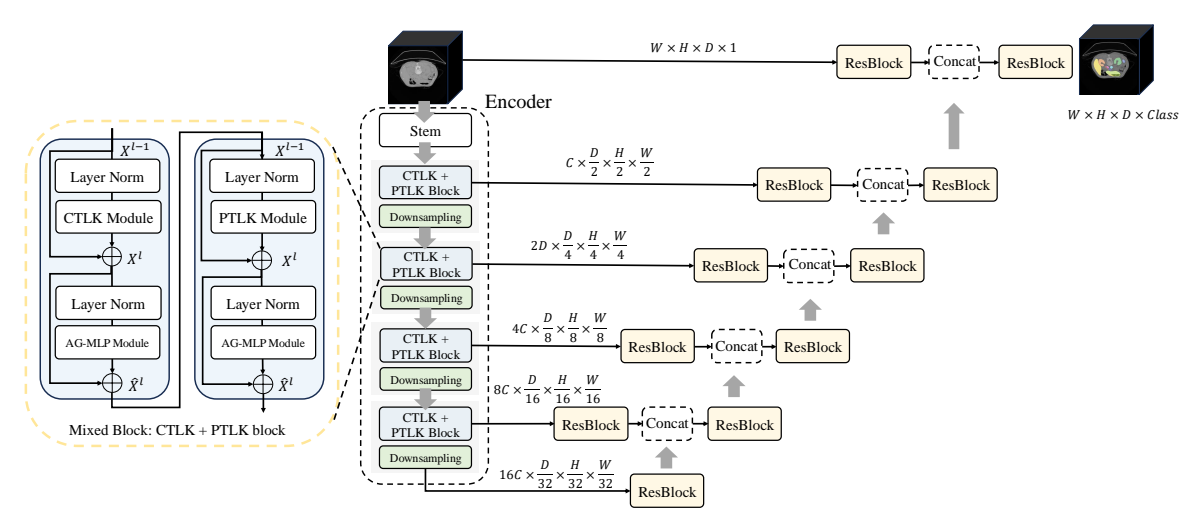


Figure 5: The architecture of the TransLK-NETR. The encoder is constructed by incorporating the mixed block (CTLK+PTLK block) into a 4-stage ViT architecture for feature extraction. Each CTLK block consists of a CTLK module and an AG-MLP module, and each PTLK block consists of a PTLK module and an AG-MLP module.

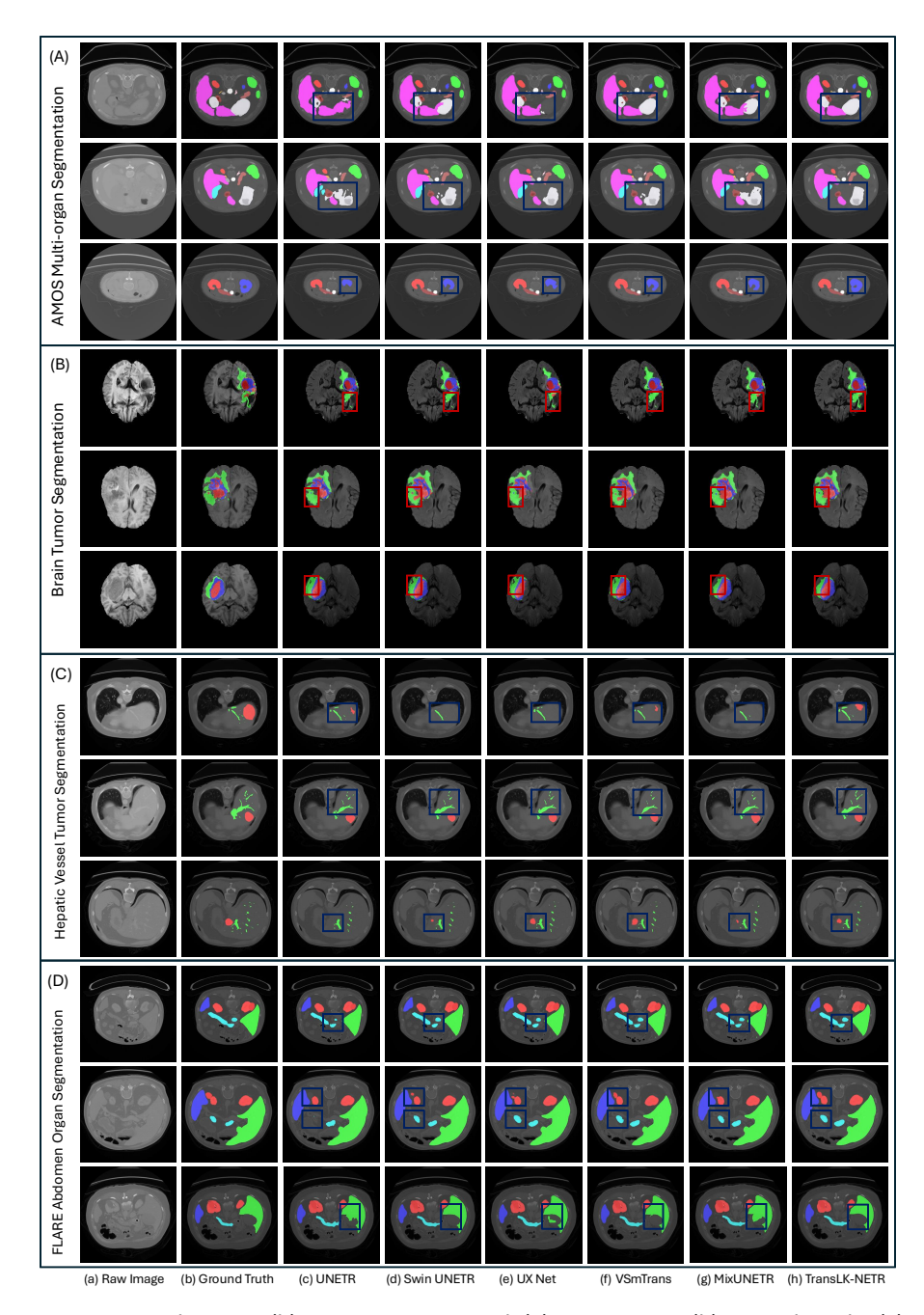


Figure 6: Qualitative comparison between (h) TransLK-NETR and (a) Raw image, (b) ground truth, (c) UNETR, (d) Swin UNETR, (e) UX Net, (f) VSmTrans, and (g) MixUNETR. Results are shown across four public datasets, including (A) the AMOS 2022 Multi-organ dataset, (B) the MSD Brain Tumor dataset, (C) the MSD Hepatic Vessel Tumor dataset, and (D) the FLARE Abdomen Organ dataset. Red and blue boxes mark the regions where TransLK-NETR demonstrates better segmentation results than other methods.

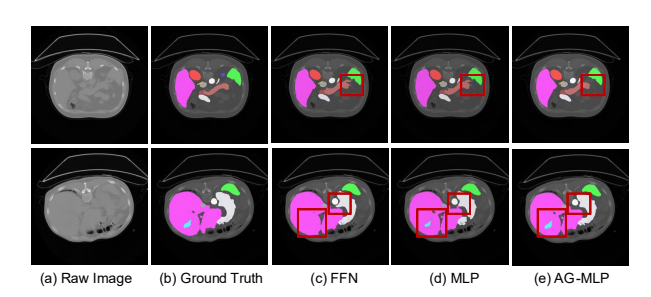


Figure 7: Qualitative comparison among TransLK-NETR when they are incorporated with (c) FFN, (d) MLP, and (e) AG-MLP on the AMOS multi-organ segmentation task. Red boxes mark the regions where TransLK-Net incorporated with AG-MLP demonstrate better segmentation results than other networks.